https://doi.org/10.5194/egusphere-2026-4431
Preprint. Discussion started: 10 August 2026

Measurement Report: Aircraft observations of secondary ice production in convective clouds over the Tibetan Plateau

Yuyan Long[1], Delong Zhao[2,3]*, Yun Zhang[1*], Dantong Liu[4], Jing Duan[2,3], and Mengyu Huang[5]

[1]College of Meteorology and Oceanography, National University of Defense Technology, Changsha, China
[2]CMA Key Laboratory of Cloud-Precipitation Physics and Weather Modification (CPML), Beijing, China
[3]CMA Weather Modification Centre (WMC), Beijing, China,
[4]Department of Atmospheric Sciences, School of Earth Sciences, Zhejiang University, Hangzhou, China.
[5]Beijing Weather Modification Center, Beijing, China.

Correspondence to: Delong Zhao (dg1828019@smail.nju.edu.cn) and Yun Zhang (zhangyun17@nudt.edu.cn)

Abstract. Secondary ice production (SIP) substantially enhances ice concentrations in clouds, thereby modulating precipitation and climate, yet underlying SIP mechanisms over the Tibetan Plateau (TP) remain poorly understood. This study investigated the observational evidence and environmental dependence of SIP in convective clouds over the TP based on aircraft observations. The SIP ratio (measured ice to estimated INP concentrations) was introduced to quantify ice enhancement. Flight observations on 6 July 2014 revealed ice concentrations reached 205.4 L^{-1} in convective clouds, with the SIP ratio peaking at 1000 near −5℃. The SIP effective temperature window extended to −16℃, substantially broader than the classical Hallett–Mossop (HM) range. Between −3℃ and −8℃, the HM process played the dominant role, accompanied by ice-ice collisional breakup (BR) and freezing droplet shattering (DS). Between −8℃ and −16℃, SIP persisted despite reduced HM efficiency, sustained by DS and BR, plus possible upward transport of supercooled large droplets and columnar crystals from warmer levels. SIP-active legs exhibited bimodal ice particle spectra with peaks below 100 μm and between 200 and 300 μm. The size of supercooled droplets dictated SIP initiation, with thresholds of approximately 24 μm above −8℃ and 200 μm below −8℃. Seven flights further indicate that temperature determined SIP occurrence and dominant mechanism, and hydrometeor concentration exhibited a pronounced positive correlation with the SIP ratio. These findings provide new insights into SIP processes in high-altitude convective clouds and important implications for improving cloud microphysical parameterizations in weather and climate models.

1 Introduction

Clouds are an important component of the Earth's system and play a crucial role in radiation budget and precipitation formation (Bony et al., 2015; Guo et al., 2015; Korolev et al., 2017). Ice particles form in clouds through both primary nucleation on ice nucleation particles (INP) and secondary ice production (SIP). Aircraft observations show that ice concentrations in mixed-phase clouds are several orders of magnitude higher than INP concentrations, which is generally attributed to SIP (Cantrell and Heymsfield, 2005; Crawford et al., 2012; Rangno and Hobbs, 2001). Understanding SIP

https://doi.org/10.5194/egusphere-2026-4431
Preprint. Discussion started: 10 August 2026

mechanisms and their environmental dependence is essential for predicting precipitation formation and assessing cloud-climate interactions (Zhao and Liu, 2021).

There are three SIP mechanisms primarily investigated in field observations and numerical simulations (Field et al., 2017; Korolev and Leisner, 2020). The most widely studied is the Hallett–Mossop (HM) process, also known as rime splintering. Between –3°C and –8°C, ice particles collide with supercooled droplets during the riming process, producing numerous columnar small ice crystals (Hallett and Mossop, 1974; Mossop, 1985). The existence of the HM process has been confirmed by numerous in situ observational studies (Crosier et al., 2011; Grosvenor et al., 2012; Hou et al., 2021; Huang et al., 2008, 2011; Yang et al., 2014). However, recent observations indicate that the HM process can extend beyond the traditional temperature range through the seeder-feeder mechanism (Du et al., 2024). Beyond the HM temperature range, the freezing droplet shattering (DS, Leisner, 2014) and ice-ice collisional breakup (BR, Takahashi et al., 1995; Vardiman, 1978) mechanisms may also play a significant role in enhancing ice concentrations in clouds. Korolev et al. (2020) noted that the DS mechanism is strongly supported by aircraft observations. Remote sensing analyses of Arctic mixed-phase clouds further suggest that DS may promote SIP more efficiently than the HM process (Luke et al., 2021). Sotiropoulou et al. (2020) found only the combination of HM and BR can explain the observed high ice concentrations.

However, multiple SIP mechanisms may coexist within clouds, rather than operating independently (Hou et al., 2023; Long et al., 2025). However, it remains difficult for current observational methods to distinguish and quantify the specific contributions of individual mechanisms. Numerical modeling studies provide an important perspective for this purpose. Modeling studies (Han et al., 2024; Waman et al., 2022) indicate that BR is the dominant SIP mechanism in mature convective clouds. Huang et al. (2022) further quantified the contribution rates of different SIP mechanisms using the WRF model. Their results show that in the strong updraft core regions with abundant liquid water within deep convective systems, ice crystal formation was dominated by HM process (at –5°C) and DS (between –5°C and –20°C), with a combined contribution rate exceeding 58%, while BR dominated in other regions. Nevertheless, large uncertainties still exist in the understanding of SIP mechanisms due to the high complexity of cloud dynamical and microphysical processes, as well as differences in parameterization schemes.

The Tibetan Plateau (TP), with a mean elevation exceeding 4000 m, stands as the highest and most extensive highland in the world. Known as the Third Pole, the TP exerts profound thermal and dynamic influences on regional and global climate systems (Kang et al., 2010; Liu and Chen, 2000; Qiu et al., 2019; Suo et al., 2023). However, the microphysical processes within summer convective clouds over the TP remained elusive due to the paucity of direct observational investigations. To address this observational gap, the Third Tibetan Plateau Atmospheric Scientific Experiment (TIPEX-III) was conducted in the summer of 2014, providing valuable ground-based and aircraft observation data for investigating cloud systems over the TP. Using ground-based millimeter cloud radar, unimodal distributions of both ice and liquid cloud microphysical properties were identified over the TP, with distinct relationships between ice effective radius, ice water content (IWC), and temperature in high-level ice clouds, as well as increasing trends of droplet effective radius and liquid water content (LWC) with height in low-level liquid clouds (Zhao et al., 2016, 2017). Zhao et al. (2018) reviewed the major achievements of

https://doi.org/10.5194/egusphere-2026-4431
Preprint. Discussion started: 10 August 2026

TIPEX-III, revealing that cloud droplet concentrations over the TP were considerably lower than those over pristine oceanic regions. Aircraft observations during this campaign further demonstrated that characteristic cloud droplet number concentrations were approximately 1–2 orders of magnitude lower than those observed over other continental and oceanic regions (Chang et al., 2019). Additionally, these studies found that TP clouds contain substantial amounts of supercooled liquid water, which promotes active glaciation and riming processes, consequently resulting in elevated graupel particle concentrations. More recently, Zhao et al. (2023) utilized TIPEX-III aircraft observations to demonstrate that the HM process was identified as the dominant SIP mechanism contributing to ice enhancement in convective clouds over the TP.

Previous SIP studies have consistently focused on the identification of the HM process within traditional temperature range, yet there has been little investigation into other SIP mechanisms over the TP. The purpose of this study is to investigate the distributions of different SIP mechanisms and dependence in convective clouds over the TP using aircraft observations from TIPEX-III. The remainder of this paper is organized as follows. Section 2 introduces data and methods, including aircraft instrumentation, cloud phase classification, and the calculation of SIP ratio. Section 3 presents the observational results, beginning with an overview of the research flights, followed by observational evidence of SIP in both the classic HM temperature range and beyond, and the dependence of SIP ratio on environmental and cloud conditions. Section 4 discusses the comparison with other regions and the limitations of this study, and Section 5 summarizes the conclusions.

2 Data and methods

2.1 Instrumentation

This study utilized the King Air 350 aircraft equipped with a comprehensive suite of in-situ microphysical probes (Table 1) to characterize cloud microphysics and meteorological parameters. The Passive Cavity Aerosol Spectrometer Probe (PCASP, DMT Inc.) is a passive cavity-type aerosol particle scattering probe that is divided into 30 bins and detects aerosol particles that are mainly in the range of 0.1–3 μm. The Fast Cloud Droplet Probe (FCDP, SPEC Inc.) measures the size and concentration of cloud droplets by measuring the light scattering caused by their interaction with a laser beam (Lance et al., 2010). The instrument can measure particles with a particle size of 2 to 50 μm, with a resolution of 3 μm.

Three imaging probes were employed to capture particle images across different size ranges. The Two-Dimensional Stereo probe (2DS, SPEC Inc.) is composed of two diode laser beams crossed at right angles to illuminate two linear 128 photodiode arrays and measure particle size and number concentration (Lawson et al., 2006). The 2DS operates in two configurations. 2DS10 measures 10–1280 μm particles at 10 μm resolution, while 2DS50 covers 50–6400 μm at 50 μm resolution. In this study, the 2DS data have been corrected for particle shattering and out-of-focus effects.The Three-View Cloud Particle Imager (3V-CPI, SPEC Inc.) integrates 2DS and CPI capabilities to measure 10–6400 μm particles, overcoming uneven sensitivity errors for less than 100 μm particles to capture droplet and ice particle size, shape, and phase for CPI (Glienke et al., 2020). The High Volume Precipitation Spectrometer (HVPS, SPEC Inc.) adopts 2DS optoelectronic

https://doi.org/10.5194/egusphere-2026-4431
Preprint. Discussion started: 10 August 2026

technology with 128 photodiodes to image large precipitation particles from 150 μm to 19200 μm, and is equipped with temperature regulation for anti-fogging in cold conditions (Korolev and Isaac, 2005).

The Nevzorov Probe is a thermostatic hotwire probe designed for measuring IWC and LWC in clouds (Korolev et al., 1998). It consists of two probes (hotwire and deep conical total water meter) to measure liquid water content and total water content respectively. The Aircraft Integrated Meteorological Detection System (AIMMS-20) can be used for the observation of temperature, humidity, 3D spatial conditions of wind, and airflow during flight. Local Standard Time (LST, UTC+8) was used in this study.

Table 1. Instrument introduction.

Instruments	Parameters	Range	Resolution
FCDP	The size and concentration of cloud droplets	2–50 μm	3 μm
2DS10	The size, shape and concentration of	10–1280 μm	10 μm
2DS50	ice crystal particles	50–6400 μm	50 μm
3V-CPI	The size, shape, and content of water droplets and ice particles	10–6400 μm	10 μm
HVPS	The size, shape and concentration of precipitation particles	150–19200 μm	150 μm
PCASP	Aerosol particles	0.1–3 μm	0.01–0.2 μm
Nevzorov Probe	Liquid and total water content	0.005–3 g m^{-3}	0.005 g m^{-3}
AIMMS-20	Location, altitude, temperature, humidity, wind	–	–

2.2 Classification of cloud phase

Ice and liquid particles in the 2DS data were separated with Optical Array Shadow Imaging System developed by the University of Manchester. Following Crosier et al. (2011), the algorithm uses the circularity metric $C = P^2/(4\pi A)$, where P and A are the perimeter around the edge of the particle and the total area of the particle, respectively. Images with $0.9 \le C < 1.2$ were classified as round particles (drizzle), whereas images with $C \ge 1.2$ were classified as irregular particles (ice).

Cloud phase was classified from the IWC-to-LWC ratio and the particle categories. Samples with IWC/LWC > 10 and irregular particle concentrations from 2DS10 more than 10 L^{-1} were classified as ice cloud. The remaining samples were classified as liquid water cloud and subdivided into small water cloud (maximum droplet diameter smaller than 20 μm), large water cloud (round particle concentrations from 2DS more than 10 L^{-1}), and middle water cloud (all remaining liquid water samples).

https://doi.org/10.5194/egusphere-2026-4431
Preprint. Discussion started: 10 August 2026

2.3 Calculation of the SIP ratio

The SIP ratio is introduced in this study as a dimensionless diagnostic of the magnitude of observational ice enhancement, following the ice multiplication factor (Wieder et al., 2022). It is defined as the ratio of ice particle number concentrations measured by aircraft from 2DS10 (N_{ice}) to INP concentrations (N_{INP}):

$$\text{SIP ratio} = \frac{N_{ice}}{N_{INP}} \tag{1}$$

In this study, the INP concentrations in the atmosphere were not measured separately. Therefore, the N_{INP} (L^{-1}) was estimated from the concentration of aerosols outside clouds with size larger than 0.5 μm ($N_{a,0.5}$, cm^{-3}), following the empirical parameterization proposed by DeMott et al. (2010):

$$N_{INP} = a(273.16 - T)^{b}\left(N_{a,0.5}\right)^{c(273.16-T)+d} \tag{2}$$

where T is temperature (K), a = 0.0000594, b = 3.33, c = 0.0264, and d = 0.0033.

3 Results

3.1 Flight overview and general conditions

The TIPEX-III aircraft observations were conducted near the Naqu radar site in the central TP, which lies in a valley at approximately 4500 m and is surrounded by terrain above 5000 m. Fig. 1 shows seven flight tracks from 06 to 24 July 2014 (20140706, 20140709, 20140713, 20140718, 20140720, 20140721, 20140724). Among them, flight 20140706 provided the most complete collocated microphysical sampling and was selected for the detailed process-oriented case analysis in Sect. 3.2. The pooled analysis in Sect. 3.3 uses observations from all seven flights as descriptive campaign context. Fig. 2a presents satellite FY-2D visible-band cloud image on 06 July 2014, showing vigorous convection over the TP with mesoscale convective cloud clusters in the aircraft observation region characterized by bright white cloud tops and deep vertical development. The composite radar reflectivity from the Naqu radar further reveals that the aircraft penetrated the core region of the convective systems and performed multiple sampling passes near the strong echo center, with core reflectivity exceeding 30 dBZ (Fig. 2b).

https://doi.org/10.5194/egusphere-2026-4431
Preprint. Discussion started: 10 August 2026

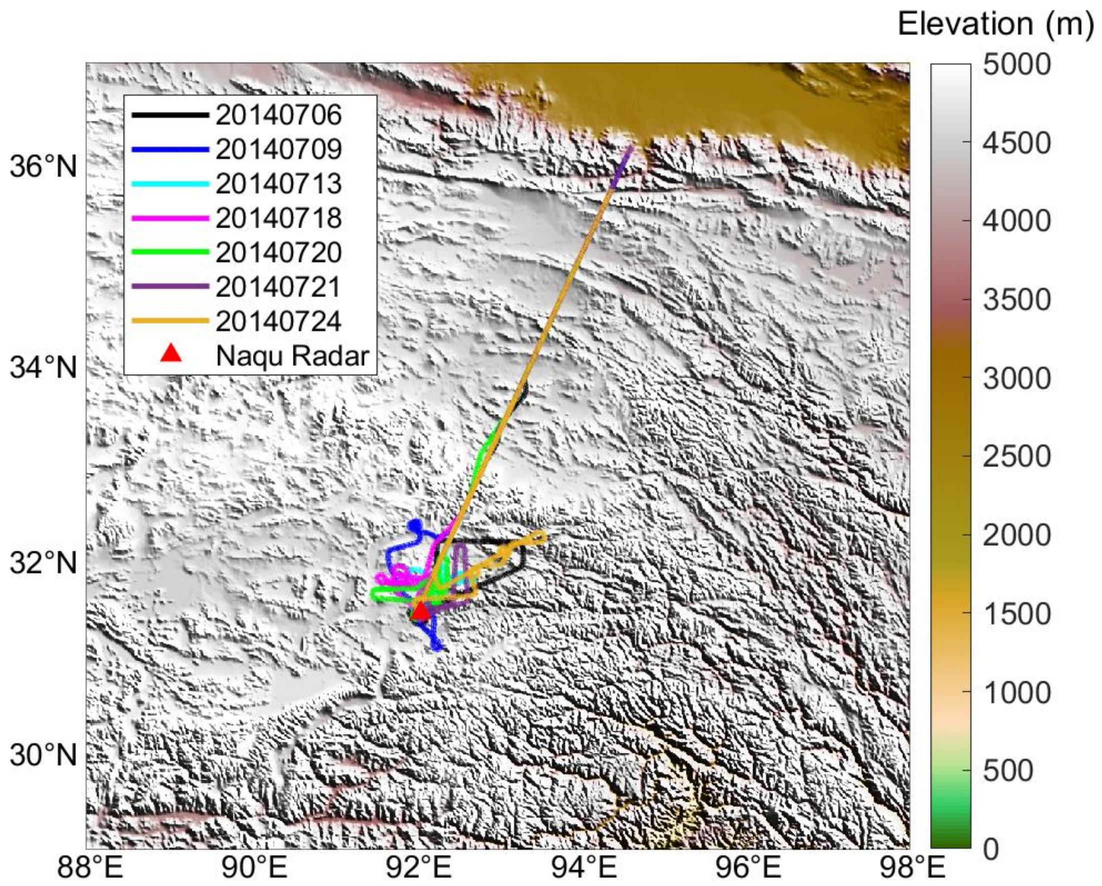

Figure 1: Terrain elevation in the observation region (shading, m) with seven aircraft tracks from 06 to 24 July 2014. The red triangle indicates the location of the Naqu radar (31.48°N, 92.06°E).

https://doi.org/10.5194/egusphere-2026-4431
Preprint. Discussion started: 10 August 2026

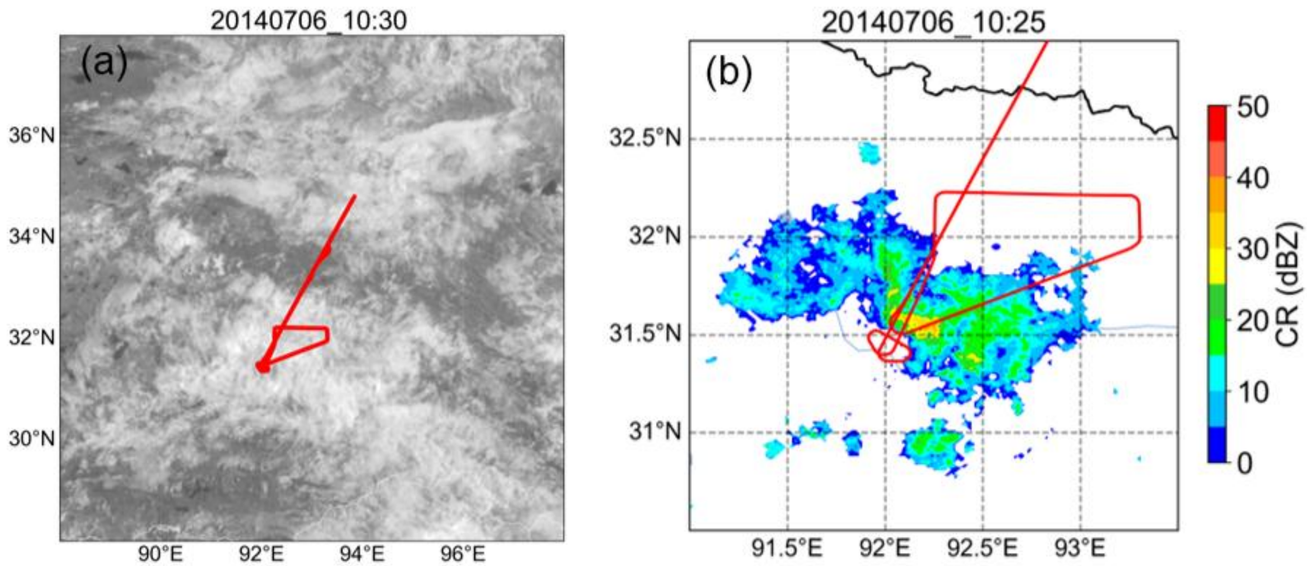

Figure 2: (a) satellite FY-2D visible-band cloud image, and (b) composite radar reflectivity from the C-band ground-based Naqu radar. The red line is aircraft track on 06 July 2014.

Fig. 3 presents droplet size distributions for typical liquid clouds observed over the TP under different cloud conditions on 06 July 2014. In small and middle water clouds, the cloud droplet size peaked at less than 20 μm, with no drizzle present (Figs. 3a-d). In large water clouds (Figs. 3e-f), the peak size reached 23.5 μm, accompanied by large drizzle with peak size at 60 μm. Notably, the convective cloud exhibited a bimodal size distribution of cloud droplet, with a maximum effective diameter of 19.4 μm (Fig. 3g). Figure 4a quantifies the proportion of cloud droplets larger than 20 μm in the three liquid cloud types on 06 July 2014. No droplets larger than 20 μm were detected in small water clouds. However, in both middle and large water clouds, the proportion of droplets exceeding 20 μm increased markedly, with large water clouds further characterized by significantly enhanced drizzle concentrations. The majority of cloud droplet sizes were concentrated in the 10–20 μm range, with some even exceeding 25 μm (Fig. 4b).

https://doi.org/10.5194/egusphere-2026-4431
Preprint. Discussion started: 10 August 2026

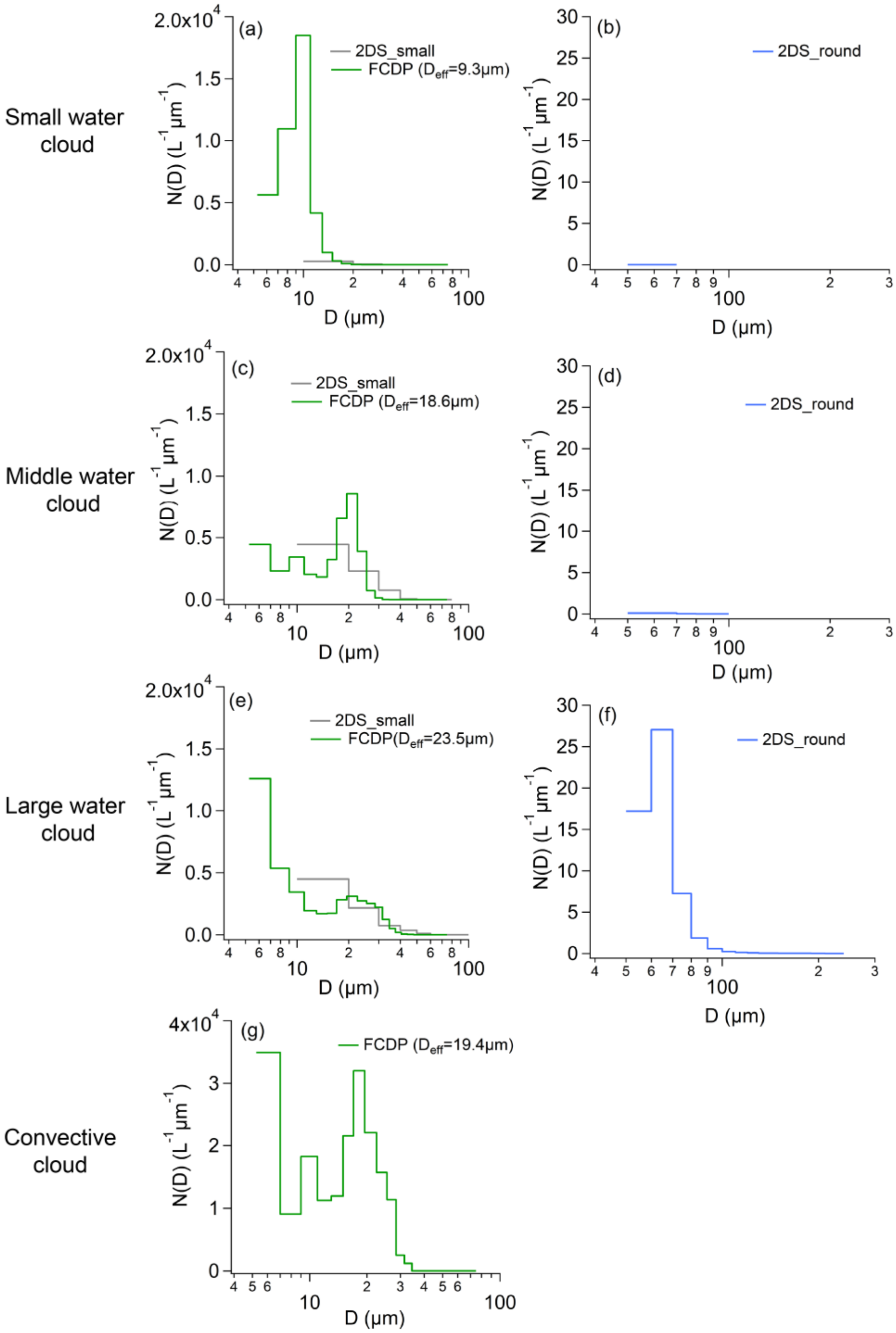

Figure 3: Droplet size distributions for typical liquid clouds observed over the TP on 06 July 2014: (a, b) small water cloud, (c, d) middle water cloud, (e, f) large water cloud, and (g) convective cloud. Green line is cloud droplet from FCDP, grey line is small droplet and blue line is drizzle from 2DS.

https://doi.org/10.5194/egusphere-2026-4431
Preprint. Discussion started: 10 August 2026

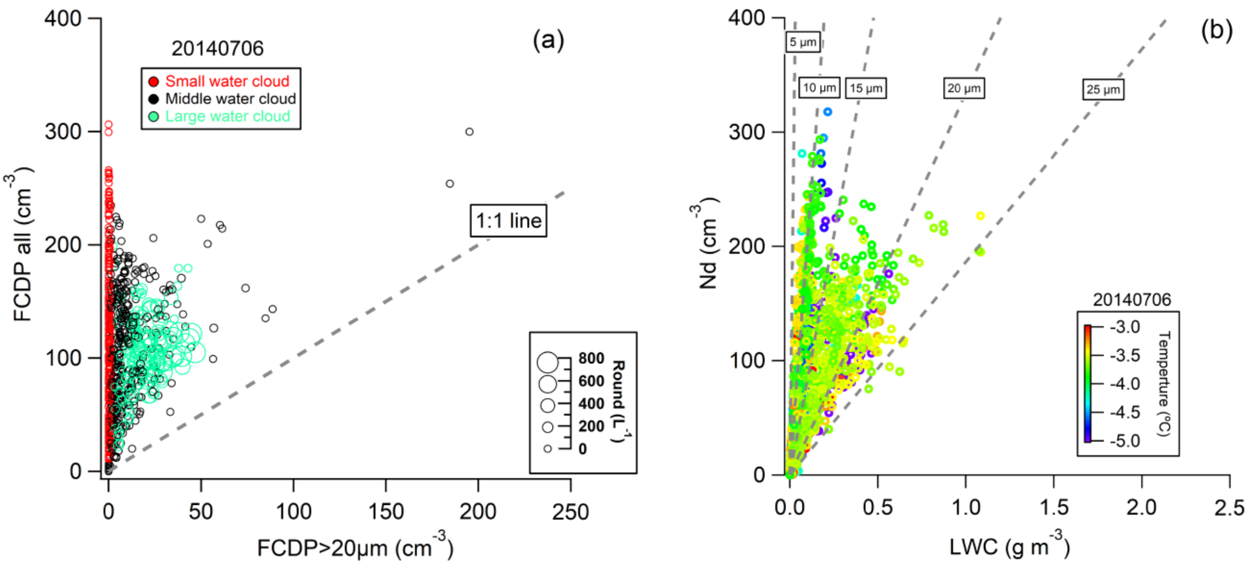

Figure 4: Dependence of cloud droplet properties measured by FCDP on 6 July 2014: (a) the concentrations of all cloud droplet versus cloud droplet larger than 20 μm on 6 July, coloured by classified clouds and sized by drizzle number concentrations; (b) all cloud droplet number concentrations versus LWC, coloured by temperature from –3℃ to –5℃. Dashed lines in panel (b) are obtained by fitting cloud droplet number concentrations and LWC correlation at the same effective diameter.

Fig. 5a shows the vertical distributions of aerosol particles (greater than 120 nm, regarded as CCN), cloud droplet concentrations, and LWC on 06 July 2014. The CCN concentrations gradually decreased with increasing altitude. Cloud droplets were mainly concentrated between 6.5 km and 7 km, with maximum cloud droplet number concentrations exceeding 300 cm^{-3}. The LWC was generally below 0.2 g m^{-3}, but increased significantly above 8.5 km (–15℃), exceeding 0.5 g m^{-3}. At this level, abundant drizzle with size greater than 50 μm was observed within the cloud (Fig. 6). The concentrations of aerosol particles greater than 500 nm were significantly lower, generally less than 4 cm^{-3} above 6 km (Fig. 5b). Interestingly, the ice concentrations on 06 July 2014 were markedly elevated, far exceeding the predicted INP concentrations (Fig. 5c), pointing to the likely occurrence of SIP.

Overall, the flight on 06 July 2014 exhibited typical background conditions favorable for SIP. This case featured broad cloud droplet spectra with abundant large droplets exceeding 20 μm and drizzle larger than 60 μm at –15℃, providing sufficient large droplet conditions for SIP. The concentrations of aerosol particles greater than 500 nm (potential INP) were notably below 4 cm^{-3}. However, ice concentrations substantially surpassed predicted INP concentrations, indicating that the high ice concentrations were not produced through primary nucleation. These characteristics of low INP concentration, high ice concentration, abundant large droplets collectively suggest that the observed high ice concentrations on 06 July 2014 likely resulted from SIP.

https://doi.org/10.5194/egusphere-2026-4431
Preprint. Discussion started: 10 August 2026

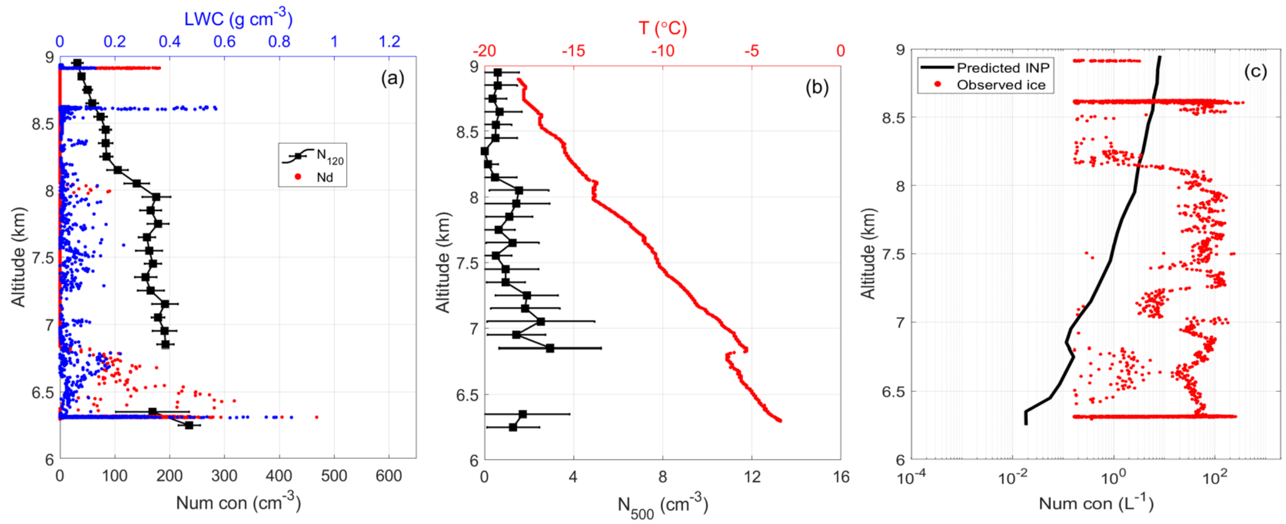

Figure 5: Vertical profiles on 6 July 2014: (a) cloud droplet number concentration (N_d, red scatter), LWC (blue scatter) and average aerosol number concentration with size larger than 120 nm (N_{120}, black scatter); (b) temperature (red scatter) and average aerosol number concentration with size larger than 500 nm (N_{500}, black scatter); (c) the concentrations of predicted INP (black line) and observed ice (red scatter).

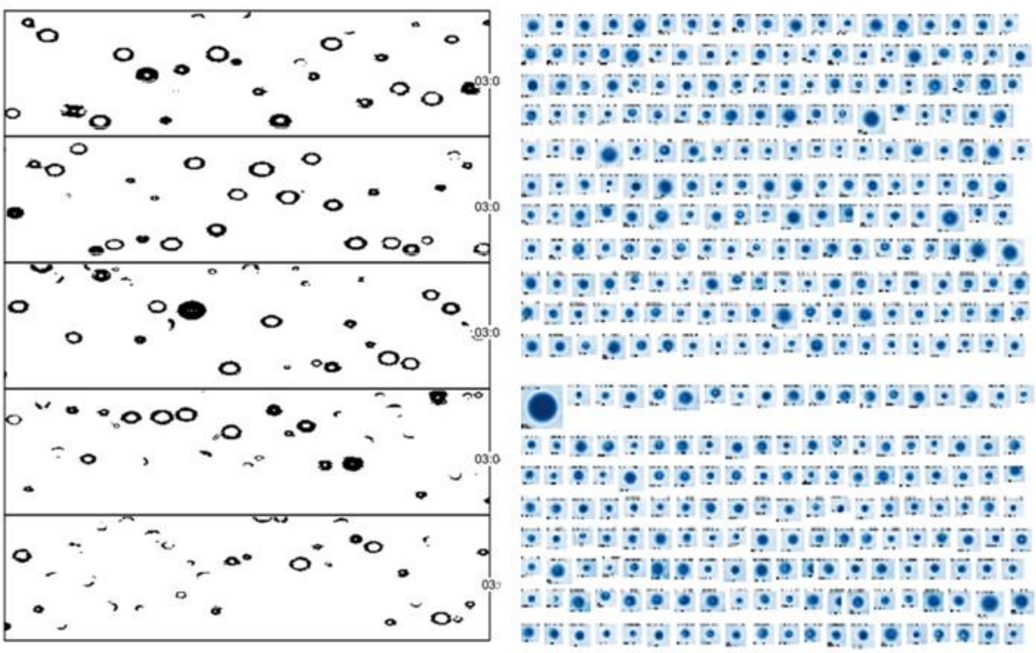

Figure 6: Example 2DS and CPI images at –15°C on 6 July 2014.

https://doi.org/10.5194/egusphere-2026-4431
Preprint. Discussion started: 10 August 2026

3.2 Evidence of secondary ice production on 06 July 2014

This study selected periods with high ice concentrations during the flight on 06 July 2014, attempting to find aircraft observational evidence of SIP. A total of 5 cases were selected from 06 July 2014 to analysis SIP. Among them, case 1 (Fig. 7), case 2 (Fig.S1) and case 3 (Fig. S3) involved straight level flight at 6.3 km near –4°C, while case 4 (Fig. 11) and case 5 (Fig. S5) were conducted at higher altitudes (from –3°C to –16°C). This section focuses on analyzing the SIP aircraft observational characteristics of case 1 and case 4, corresponding to two different temperatures: one at the classic HM temperature and another beyond.

3.2.1 Classic HM temperature (–3°C to –8°C)

Fig. 7 presents the time series of case 1 at approximately 6.3 km with temperatures between –3°C to –8°C. The six selected periods correspond to distinct cloud microphysical conditions as indicated by the vertical radar reflectivity in Fig. 7a, with notably higher reflectivity values observed in case 1.5 and case 1.6. The aircraft penetrated an embedded convective region in case 1.6. In case 1.1, the cloud was predominantly composed of supercooled liquid water with in updraft regions. The drizzle concentration exceeded 700 L^{-1}, with LWC reaching up to 5 g m^{-3}, while ice crystal number concentration remained below 10 L^{-1}. In case 1.2, characterized as a moderate water cloud, large droplets coexisted with cloud droplets, but LWC decreased compared to case 1.1. From case 1.3 to case 1.6, clouds were identified as ice-dominated. In cases 1.3 and 1.5, both cloud droplets and ice crystals coexisted; however, few droplets larger than 20 µm were detected by FCDP. After 10:26, IWC, ice crystal number concentration, and precipitation particle concentration increased significantly, accompanied by a substantial increase in effective diameter. Although vertical air motion remained relatively weak, the SIP ratio greatly exceeded 1 (Fig. 7e), with ice concentrations far surpassing predicted INP concentrations.

In cases 1.1 and 1.2 (Figs. 8a and 8b), the cloud was dominated by large cloud droplets (peak diameter more than 20 µm), with ice concentrations below 3 L^{-1}. In case 1.3, the particle spectrum broadened, ice concentrations increased to 21.4 L^{-1}, and columnar crystals were first observed. From case 1.4 onward, as the aircraft penetrated convective regions, columnar crystals became more prevalent, accompanied by the coexistence of large droplets and graupel, with SIP ratio exceeding 10. Case 1.6 exhibited peak ice concentrations of 205.4 L^{-1} and SIP ratio up to 1000, where columnar crystals, graupel, and irregular ice fragments coexisted (Figs. 8d–f), providing in situ observational evidence of the HM process. Similar HM evidence was identified in case 2 (Figs. S1-2). In case 3, the aircraft did not penetrate convective regions (Fig. S4). Although the cloud layer temperature was within HM range, neither typical in situ observational evidence of the HM nor fragile dendritic snow crystals were observed. However, droplets larger than 50 µm were present (Fig. S4). Therefore, DS mechanism likely dominated when SIP ratio exceeded 1 (cases 3.1 and 3.4). Nevertheless, due to the limited efficiency of frozen droplet shattering, ice concentrations did not increase as substantially as those observed in the convective regions of cases 1 and 2.

https://doi.org/10.5194/egusphere-2026-4431
Preprint. Discussion started: 10 August 2026

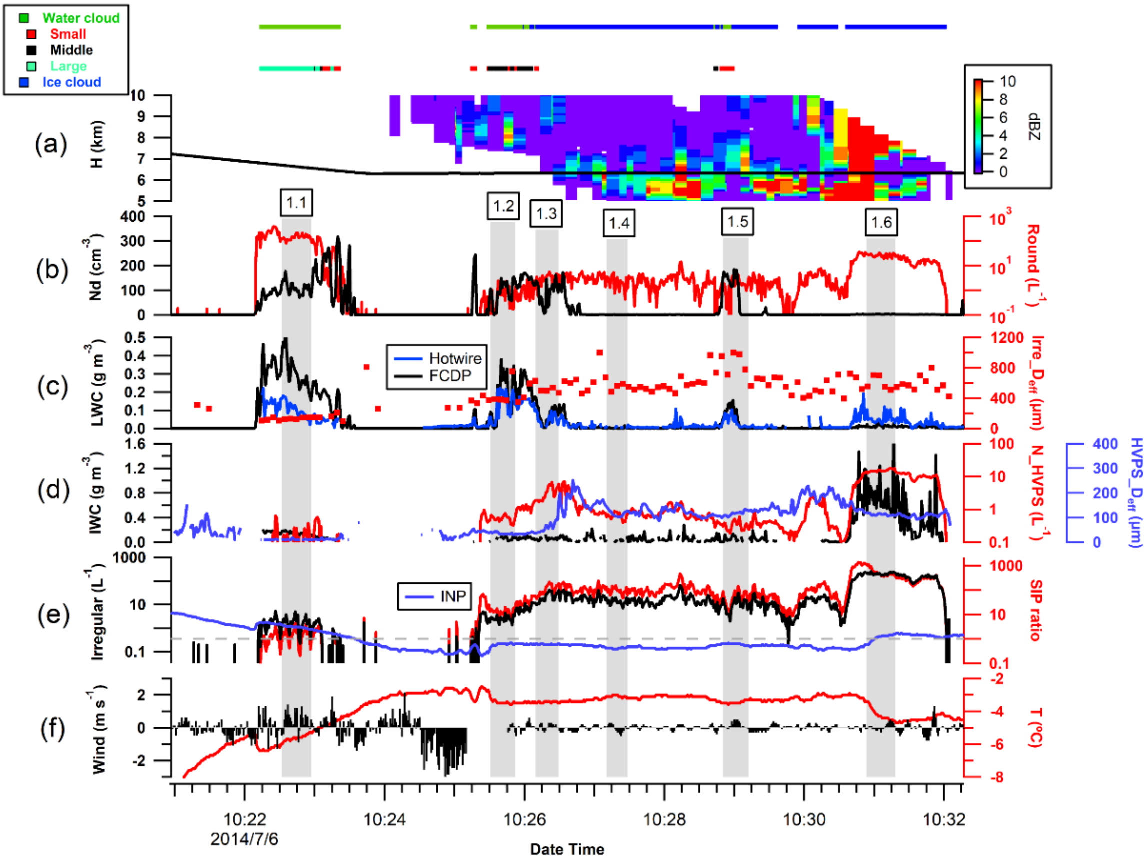

Figure 7: Time series of straight-level run pass through a series of clouds at around –4℃ in case 1 on 6 July 2014: (a) vertical profile of radar reflectivity from ground station (coloured) with flight height (black line); (b) the number concentration of cloud droplet from FCDP (black line) and round droplet (drizzle) from 2DS (green line); (c) LWC (blue line is from Nevzorov Hotwire sensor, black line is from FCDP) and effective diameter of irregular particle (red line); (d) IWC (black line), number concentration of large particle from HVPS (red line) and effective diameter from HVPS (blue line); (e) number concentration of irregular particle (black line), predicted INP (blue line) and SIP ratio (red line); (f) vertical wind speed (black line) and temperature (red line). The cloud classification is shown at the top of the figure: green bars denote water clouds, which are further categorized into small (red), middle (black), and large (cyan) water clouds; blue bars represent ice clouds.

https://doi.org/10.5194/egusphere-2026-4431
Preprint. Discussion started: 10 August 2026

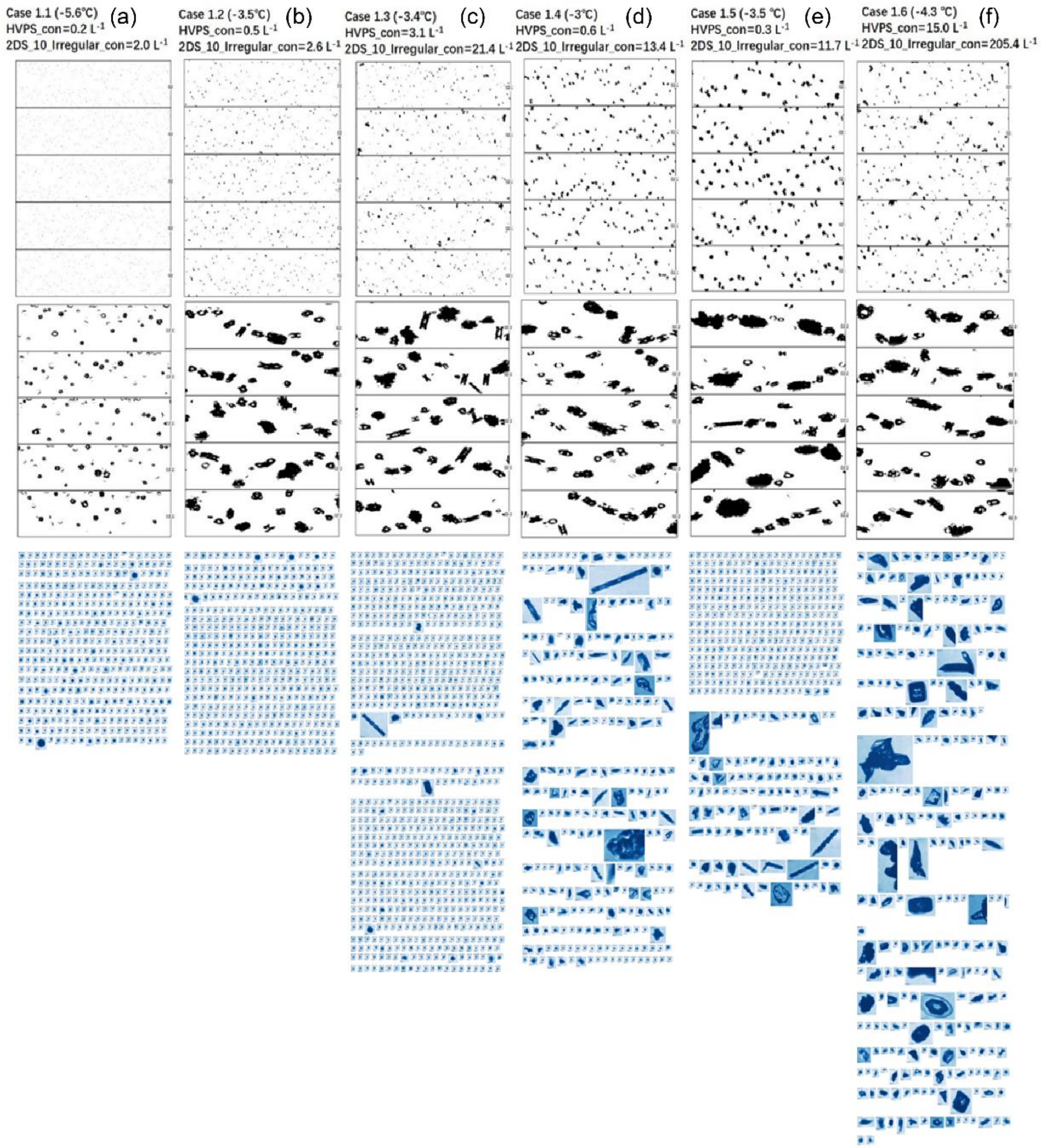

Figure 8: The example images of 2DS and CPI from –3°C to –5.6°C in case 1. The temperature and particle concentrations shown at the top of each image are average values.

225 Collectively, the observations in cases 1 and 2 show distinct signatures of the HM process, as evidenced by the abundance of columnar crystals, graupel, and large droplets within the convective regions. Ice concentrations reached up to 205.4 L^{-1}, with

https://doi.org/10.5194/egusphere-2026-4431
Preprint. Discussion started: 10 August 2026

the SIP ratio peaking at 1000, suggesting the dominant role of the HM process between –3°C and –5.6°C. In addition to the HM process, we also identified evidence of other possible SIP mechanisms. For example, the fragile structures of dendritic snowflakes observed in Fig. 9 were prone to collisions with other ice particles, suggesting the possible occurrence of the BR mechanism. Collisional breakup of ice particles near –5°C has been documented to produce fine needles and columnar fragments (Hou et al., 2023; Knight, 2012). Korolev and Leisner (2020) also noted that BR is most likely in mixed-phase convective regions. Furthermore, the images of fragmenting frozen droplets in Fig. 9 provided in situ observational support for DS. Therefore, multiple SIP mechanisms may have collectively contributed to ice enhancement in the convective regions of cases 1 and 2. In contrast, case 3 remained within the same HM temperature range (approximately −4°C), but lacked typical HM microphysical signatures. Nevertheless, ice concentrations ranged from 10 L^{-1} to 100 L^{-1}, drizzle concentrations can up to 100 L^{-1}, and the SIP ratio exceeded 1 in cases 3.1 and 3.4 (Fig. S3). In case 3, only large supercooled droplets (D > 50 μm) were present, yet no columnar crystals or graupel were detected from images (Fig. S4). Laboratory studies have shown that large supercooled droplets during freezing can produce numerous ice splinters (Lauber et al., 2018; Wildeman, 2017), and aircraft observations have demonstrated that the DS can occur effectively without riming (Korolev et al., 2020). Therefore, the DS alone may have contributed to ice enhancement under the conditions observed in case 3.

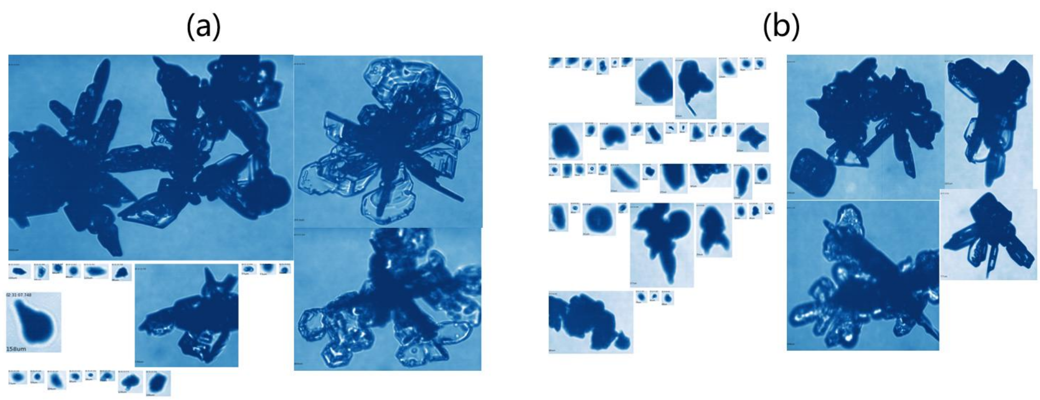

Figure 9: Example CPI images of panel (a) case 1 and panel (b) case 2.

However, a key question remains: is it the concentration or the size of supercooled droplets that critically determines SIP occurrence? To address this, we present the mean size distributions of ice particles and droplets for cases 1 to 3 in Fig. 10. All legs where SIP occurred exhibited bimodal size distributions of ice particles (Fig. 10, left panels), with the first peak at diameters smaller than 100 μm and the second peak between 200 and 300 μm. The small-mode peak (D < 100 μm) is characteristic of freshly generated secondary ice crystals, consistent with previous field studies (Crosier et al., 2011; Korolev et al., 2020). The larger mode (200–300 μm) likely corresponds to graupel or partially rimed particles that act as rimers in the HM process or as collisional partners in the BR process. The presence of this bimodal structure across different temperatures provides supporting evidence of SIP. The corresponding droplet size distributions (Fig. 10, right panels) reveal a clear contrast between SIP-active and SIP-inactive legs. In the classic HM temperature range (−3°C to −8°C), droplets larger than

https://doi.org/10.5194/egusphere-2026-4431
Preprint. Discussion started: 10 August 2026

24 μm are generally sufficient to trigger SIP, as exemplified by case 3 (Figs. 10e and 10f), where moderate ice enhancement occurred even without graupel or columnar crystals. These cases demonstrate that droplet size controls SIP initiation, with the HM process requiring droplet size more than 24 μm in the presence of rimers, whereas the DS requires larger droplet size more than 50 μm and yields lower enhancement.

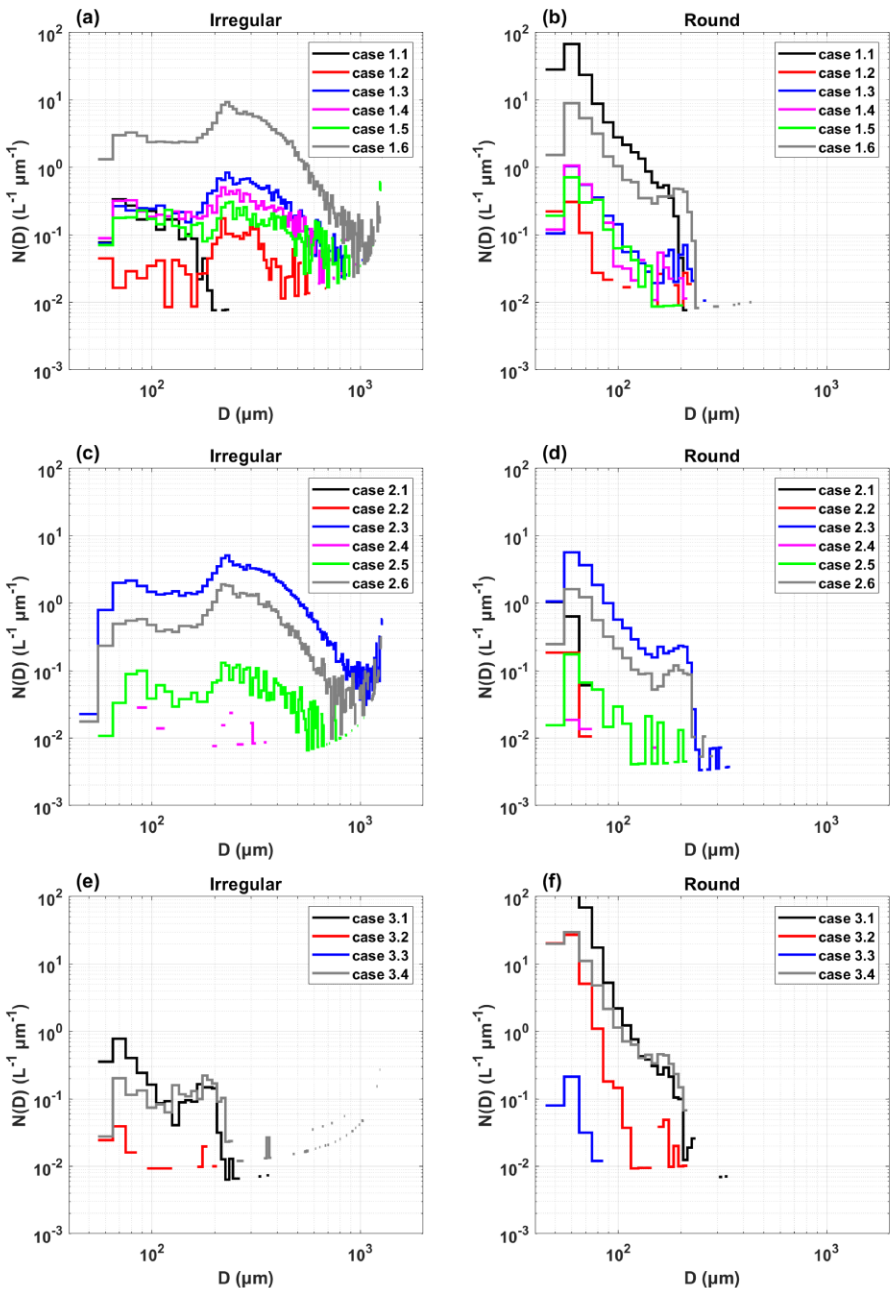

Figure 10: Mean size distributions of ice particles (left) and droplets (right): (a, b) case 1, (c, d) case 2, and (e, f) case 3.

https://doi.org/10.5194/egusphere-2026-4431
Preprint. Discussion started: 10 August 2026

3.2.2 Beyond HM temperature (–3°C to –16°C)

Fig. 11 presents the time series of various physical parameters in case 4, where the aircraft ascended from 6.3 km to 8.6 km, with temperatures ranging from –3.6°C to –16.3°C. Cases 4.1 and 4.2 were straight-level legs at 6.3 km, while the aircraft began climbing from case 4.3 onward. Cases 4.4 to 4.8 passed through convective regions (Fig. 11a), where LWC from the Nevzorov probe was below 0.2 g m^{-3}. Within the classic HM temperature range (cases 4.1–4.3), drizzle concentrations were 1–20 L^{-1}, precipitation particle concentrations remained below 10 L^{-1} (Fig. 12). The ice concentrations reached up to 67.7 L^{-1} and SIP ratio exceeded 100, with clear HM signatures (columnar crystals, graupel, large droplets) observed in case 4.3 (Figs. 13a–c). From cases 4.4 to 4.8, columnar crystals continued to coexist with graupel particles at temperatures colder than –8°C (Figs. 13d–f). Frozen droplets and large dendritic snowflakes were also prevalent at these low temperatures, and the SIP ratio remained above 1 down to –16°C (Fig. 11e). The HM process is known to be inefficient outside the temperature range of –3°C to –8°C (Hallett and Mossop, 1974). Griggs and Choularton (1983) suggested that an ice shell is too strong to break at temperatures colder than –8°C due to rapid growth. Therefore, this persistence of ice enhancement well beyond the classical HM temperature range raises a key question: what mechanisms sustain SIP at such low temperatures?

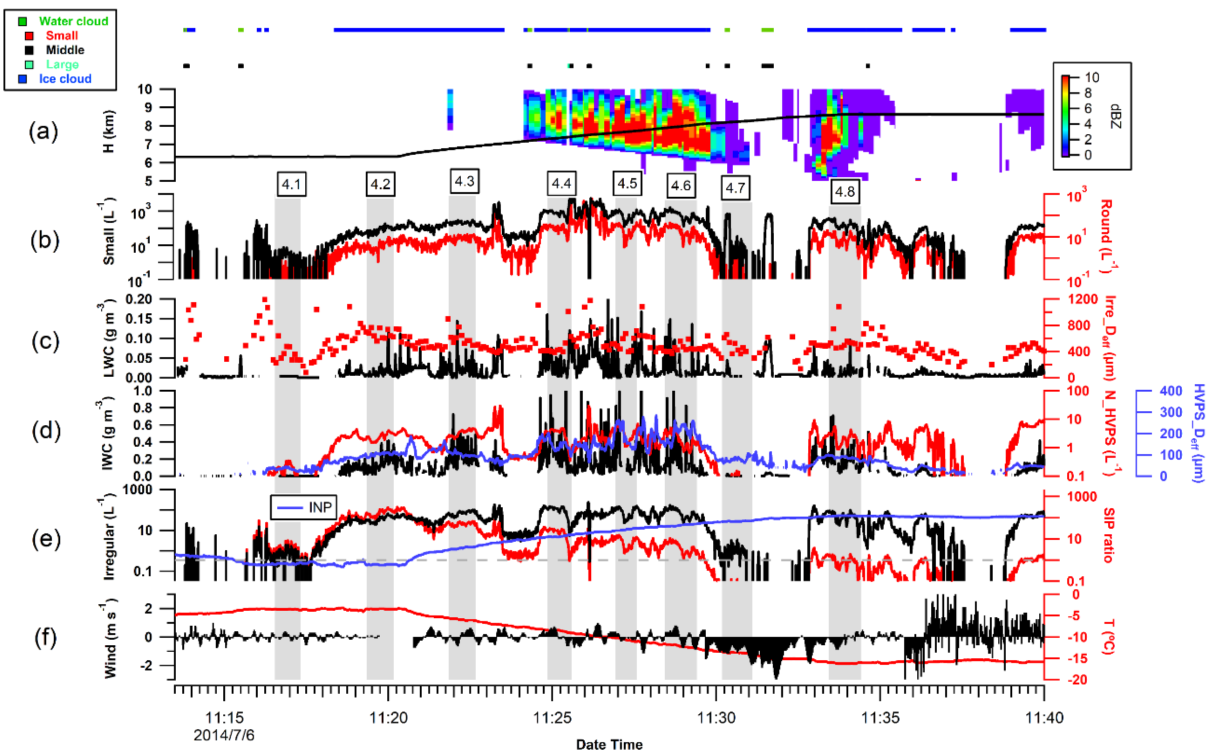

Figure 11: Time series of straight-level run pass through a series of clouds from –3°C to –16°C in case 4 on 6 July 2014: (a) vertical profile of radar reflectivity from ground station (coloured) and height (black line); (b) the number concentration of small particles from 2DS10 with size less than 80 µm (black line) and round droplet (drizzle) from 2DS (green line); (c) LWC from Hotwire (black line) and effective diameter of irregular particle (red line); (d) IWC (black line), number concentration of large particle from

https://doi.org/10.5194/egusphere-2026-4431
Preprint. Discussion started: 10 August 2026

HVPS (red line) and effective diameter from HVPS (blue line); (e) number concentration of irregular particle (black line), predicted INP (blue line) and SIP ratio (red line); (f) vertical wind speed (black line) and temperature (red line). The cloud classification is shown at the top of the figure: green bars denote water clouds, which are further categorized into small (red), middle (black), and large (cyan) water clouds; blue bars represent ice clouds.

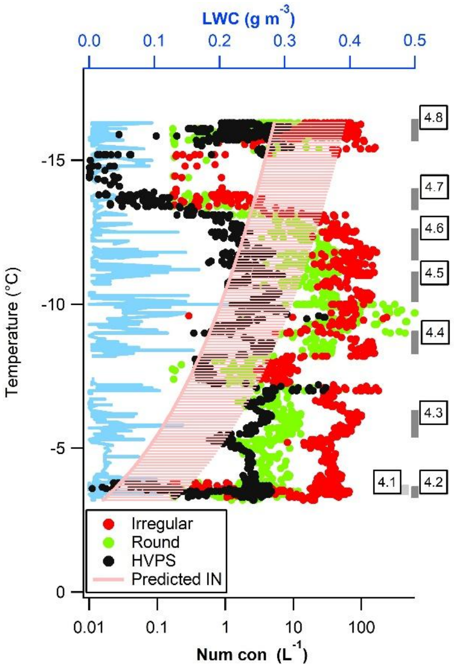

Figure 12: Vertical profiles of different particle number concentrations (bottom x-axis) and LWC (top x-axis) in case 4. The red scatters represent irregular particles, green scatters represent drizzles, black scatters represent larger particle from HVPS. The pink line shows predicted INP concentrations.

Two possible explanations can be considered. First, vertical transport of ice particles from warmer levels. Strong updrafts (approximately 3 m s^{-1}, as shown in Figs. 14b-d) could lift columnar crystals originally produced by the HM process near –5°C into the colder upper part of the cloud (up to –16°C). Bailey and Hallett (2009) noted that columnar crystals typically occur at temperatures warmer than –10°C, so their presence at –16°C strongly suggests upward transport from warmer levels. Once aloft, these columnar crystals as "seed" may continue to interact with supercooled droplets, promoting additional riming and possibly further ice fragmentation. This process would be analogous to the seeder-feeder mechanism proposed by Du et al. (2024) to explain the extension of effective SIP to –14°C in mid-latitude stratiform clouds with embedded convection. Second, in-situ SIP mechanisms (DS and BR) at low temperatures. Even below –8°C, large supercooled droplets (D > 50 μm) were still present (Fig. 13). Korolev et al. (2022) discovered the ice enhancement at low temperatures (–27°C) through aircraft measurements and pointed out that DS and BR mechanisms were plausible explanations. These mechanisms can generate secondary ice independently of vertical transport. What is more, both explanations hold true and jointly contribute to the ice enhancement at lower temperatures. But the relative contribution of each one likely depends on the local updraft

https://doi.org/10.5194/egusphere-2026-4431
Preprint. Discussion started: 10 August 2026

strength, the availability of large droplets, and the concentration of pre-existing ice particles. We must acknowledge that quantitatively distinguishing these contributions remains challenging with the current in-situ dataset.

Notably, the SIP ratio remained above 1 down to –16°C, which were substantially lower than those near –5°C (Fig. 11e). The decrease can be partly explained by the exponential increase of estimated INP concentrations at colder temperatures, and partly by the reduced efficiency of DS and BR compared to HM. In case 5, the aircraft maintained straight-level observations at 8.6 km with a temperature of approximately –16°C (Fig. S5f). The estimated INP concentration at this time was around 48 L^{-1} (Fig. S5e). The maximum ice crystal concentrations observed in the convective region of cases 5.1 and 5.3 were 128.8 L^{-1} and 97.0 L^{-1}, respectively (Fig. S5e), which was greater than the INP concentration. This may be because supercooled large droplets existed in cases 5.1 and 5.3 (Fig. S6), which could still initiate SIP, resulting in ice enhancement at –16°C. In contrast, in other legs of case 5, the average ice concentration was less than 5 L^{-1}, and SIP was not initiated.

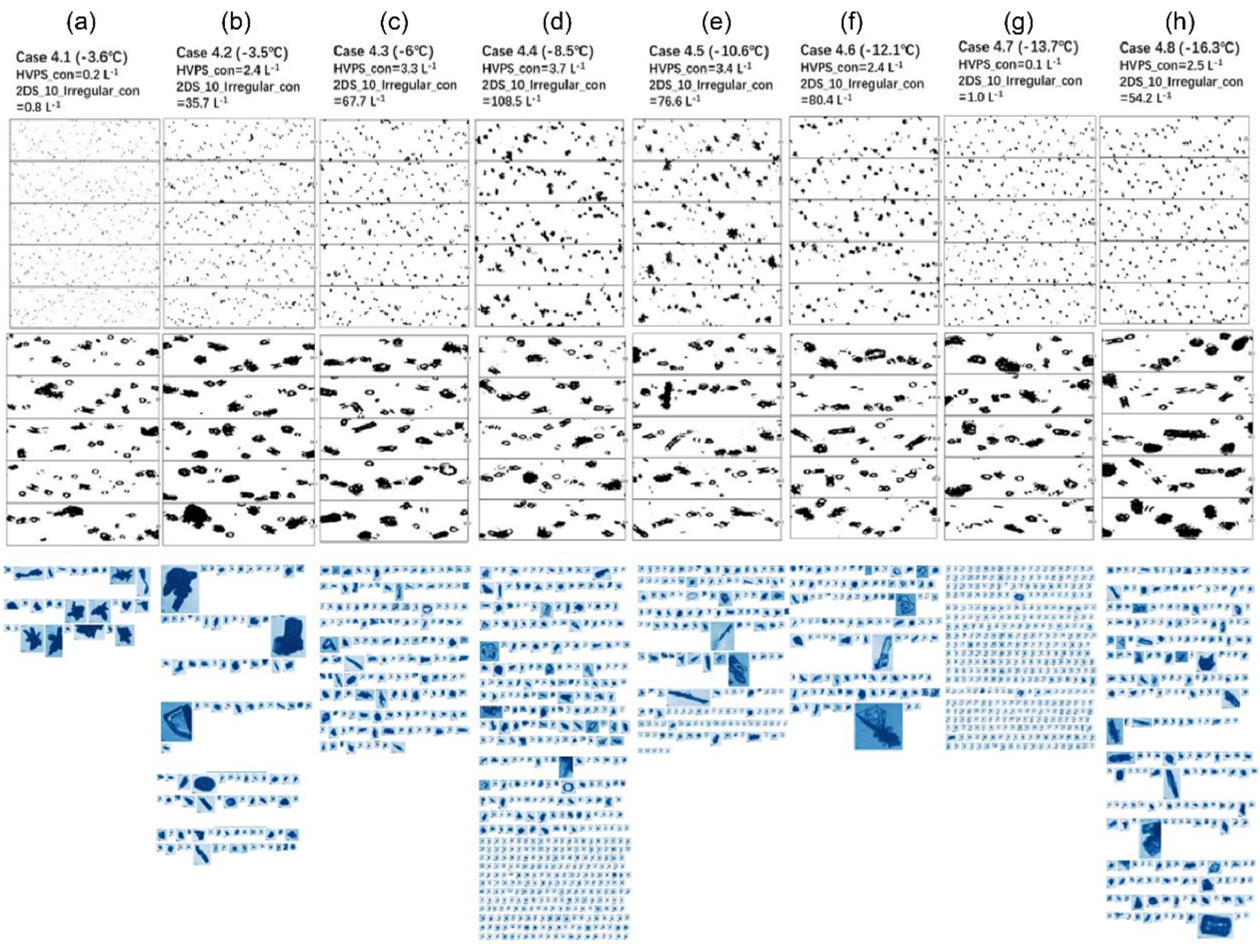

Figure 13: The example images of 2DS and CPI from –3.6°C to –16.3°C in case 4. The temperature and particle concentrations shown at the top of each image are average values.

https://doi.org/10.5194/egusphere-2026-4431
Preprint. Discussion started: 10 August 2026

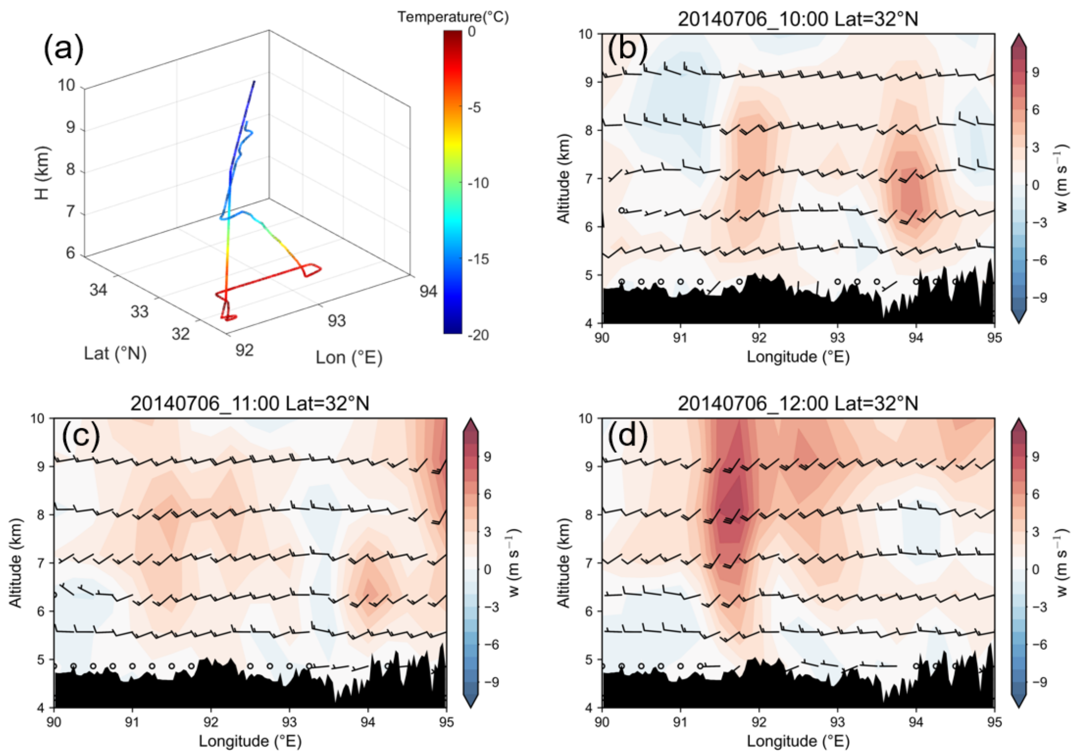

Figure 14: (a) Three-dimensional aircraft trajectory coloured by temperature; (b), (c), and (d) are vertical cross-sections along 32°N at different time, with shaded contours indicating vertical velocity and wind vectors representing the u and w wind components.

Figure 15 presents the size distributions of ice particles and droplets for cases 4 and 5. Consistent with the previous observations (cases 1 to 3), the ice particle spectra during SIP-active periods still exhibited pronounced bimodal structures. However, at temperatures below −8°C, the droplet size threshold of initial SIP becomes more stringent. The comparison between case 4.4 (high SIP activity) and case 5.6 (no SIP) is particularly instructive. In case 5.6 (Figs. 15c and 15d), although the concentration of droplets smaller than 100 μm exceeded 100 L^{-1}, droplets larger than 200 μm were nearly absent. Consequently, no SIP evidence was observed and ice concentrations remained low in case 5.6. In contrast, the droplet size distribution of case 4.8 exhibited a pronounced bimodal pattern, with large droplets of approximately 200 μm (Fig. 15b). Thus, even at a relatively low temperature, SIP was initiated and maintained relatively high ice concentrations (54.2 L^{-1}), which was even higher than that of case 4.2 (Fig. 15a), despite case 4.2 being within the HM temperature range. This contrast demonstrates that supercooled droplet size, rather than concentration alone, is the primary controlling factor for SIP at low temperatures.

https://doi.org/10.5194/egusphere-2026-4431
Preprint. Discussion started: 10 August 2026

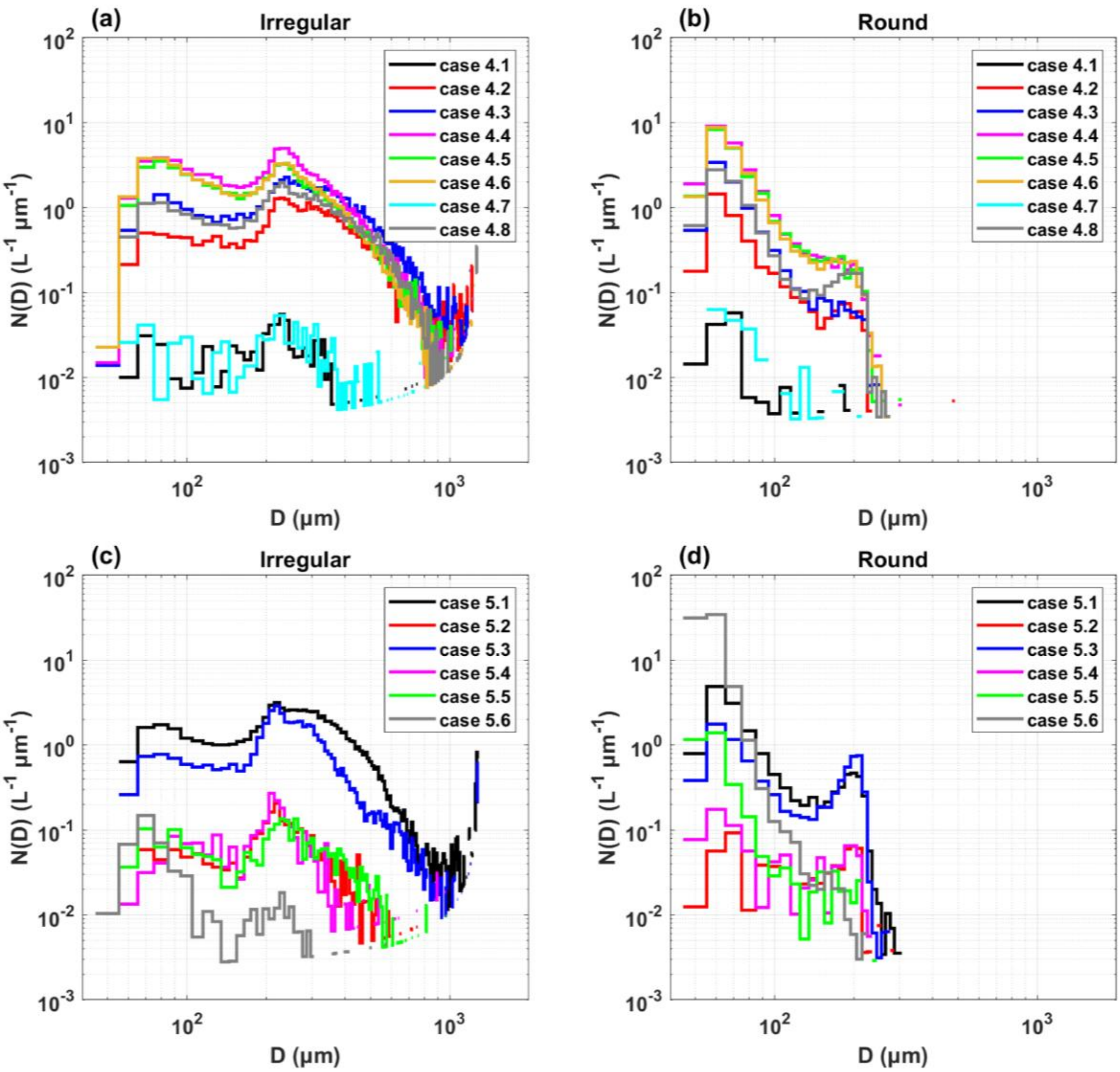

325 **Figure 15: Mean size distributions of ice particles (left) and droplets (right): (a, b) case 4 and (c, d) case 5.**

The five cases analyzed above, together with the general conditions described in Section 3.1, collectively demonstrate the key characteristics of SIP in the 6 July 2014 convective cloud system over the TP. SIP occurred across a broad temperature window from −3℃ to −16℃. In the classic HM range (−3℃ to −8℃), HM dominated in convective regions where columnar crystals, graupel, and large supercooled droplets coexisted (cases 1 and 2), accompanied by DS and BR. When graupel was absent, DS alone produced moderate enhancement with larger droplets (case 3). At temperatures below −8℃, HM became inefficient, yet SIP persisted through DS and BR, potentially augmented by upward transport of ice particles and large droplets from warmer levels via strong updrafts. All SIP-active legs exhibited bimodal ice particle spectra with peaks below 100 μm (fresh secondary ice) and between 200–300 μm (rimers or collisional partners), providing robust observational evidence of SIP. Droplet size critically controlled SIP initiation, with distinct thresholds in different temperature regimes: in the warm region (−3°C to −8°C), HM required droplets (D > 24 μm) with graupel present, whereas DS required larger droplets (D > 50 μm); in the cold region (below −8°C), the threshold became more stringent, with DS requiring droplets (D > 200 μm) to sustain SIP. These case-specific findings motivate the systematic statistical analysis across all seven flights to validate the dual regulation of temperature and hydrometeor concentrations, as presented in Section 3.3.

3.3 Quantitative dependence of SIP on temperature and hydrometeors

The above analysis of size distributions suggests that both temperature and the concentrations of different hydrometeors are likely to modulate the intensity of ice enhancement. To quantitatively examine these dependences across the entire flight, we conducted a statistical analysis of the seven aircraft observations. Fig. S7 presents an overview of aerosol and cloud microphysical characteristics across the seven flights. The TP region is characterized by a clean aerosol background, with the values of N_{500} (potential INP) generally below 10 cm^{-3} (Fig. S7d), which is considerably lower than typical continental values. However, aircraft observations revealed significantly enhanced ice number concentrations, with high values primarily concentrated between −5°C and −15°C, reaching maxima of 100–200 L^{-1}. These observed concentrations far exceed the INP concentrations estimated from the DeMott parameterization. This substantial discrepancy indicates that ice crystal formation is not dominated by traditional primary nucleation, but rather by SIP mechanisms. SIP-active regions were accompanied by abundant supercooled liquid water (LWC up to 0.2–0.5 g m^{-3}) and relatively large cloud droplets (effective diameters frequently exceeding 24 μm), which provide essential microphysical conditions for SIP mechanisms such as HM and DS. Furthermore, ice enhancement extended to regions warmer than −5°C and colder than −15°C, and significant enhancement was even observed down to −20 to −15°C in some flights. These findings demonstrate that the effective temperature window for SIP in convective clouds over the TP is substantially broader than the classical HM range, with DS and BR mechanisms sustaining SIP activity at lower temperatures, while strong updrafts may transport ice crystals produced in warmer regions to upper levels, further extending the vertical influence of SIP.

Fig. 16 illustrates how the SIP ratio varied with the number concentrations of drizzle, ice particles, and large precipitation particles under different temperature conditions based on the seven flights. Fig. 16a shows that drizzle concentrations exhibited a pronounced positive correlation with the SIP ratio. A closer look reveals an interesting feature: within the classic HM temperature range, when the drizzle concentration exceeded 100 L^{-1}, the SIP ratio only reached about 10 instead of the peak value of 1000. In fact, sustaining the HM process requires not only abundant large droplets but also sufficient rimers (or graupel). Extremely high drizzle concentrations often occur in strong updraft cores, where ice crystals and graupel may still be developing, leading to limited collision efficiency between drizzle and graupel. Consequently, when drizzle is overwhelmingly abundant but graupel is relatively scarce, the SIP ratio remains at a moderate level (around 10). Notably, even under relatively low temperature conditions (below −15°C), the SIP ratio can still exceed 1 when large amounts of drizzle are present. Together with the positive correlation between ice and drizzle concentrations at low temperatures shown in Fig. 16d, these findings indicate that the presence of drizzle can initiate SIP. Therefore, the DS mechanism plays a major role in ice enhancement at low temperatures.

https://doi.org/10.5194/egusphere-2026-4431
Preprint. Discussion started: 10 August 2026

Moreover, ice concentrations also show a strong positive correlation with the SIP ratio (Fig. 16b). Increased ice concentrations further enhance the SIP ratio, which is likely attributable to the BR mechanism, by which ice particles collide and fragment to generate additional small ice crystals. Furthermore, precipitation particle concentration is positively correlated with the SIP ratio (Fig. 16c). Specifically, large particles such as graupel and snowflakes provide essential target particles for the HM and BR processes, facilitating the occurrence and maintenance of SIP. This is consistent with the findings of Long et al. (2025), which showed that an increase in large size particles within clouds can promote SIP.

In addition to the modulation by hydrometeor concentrations, temperature itself plays a dominant role in regulating SIP. As shown in Fig. 16, when temperatures approached −5°C, the SIP ratio was generally greater than 1, with peak values reaching 1000. This indicates ice concentrations up to three orders of magnitude greater than estimated INP concentrations, consistent with the peak temperature for HM activity (Hallett and Mossop, 1974). As temperatures decreased to approximately −10°C, the SIP ratio approached 1, suggesting that the observed ice concentrations are comparable to the estimated INP concentrations. On the premise that the parameterized INP concentrations represent the actual number of activated INP under sufficient water vapor supply, this equivalence implies negligible contributions from SIP. Thus, ice crystals originate almost entirely from the activation of INP. At temperatures below −15°C, the SIP ratio fell substantially below 1, indicating that the observed ice concentration was significantly lower than the estimated INP concentration. However, this low SIP ratio does not merely reflect the absence of SIP. More importantly, it may suggest that primary nucleation itself was severely suppressed. The DeMott parameterization derived from mid-latitude and oceanic data may overestimate INP concentrations over the TP, especially at low temperatures, due to extremely low aerosol loading. Moreover, even when INP are present, their activation requires sufficient water vapor and supercooled liquid water. In the cold regions of convective clouds, water vapor was frequently depleted by ice particle growth, and the LWC remained low (Fig. 12), thereby preventing INP activation.

In summary, the combined analysis of Figs. 10, 15 and 16 demonstrates that supercooled droplets play an essential role in SIP initiation and maintenance. Droplet size determines whether SIP can initiate, with a warm-range threshold of about 24 μm and a cold-range threshold of about 200 μm. Droplet concentrations modulate the magnitude of ice enhancement. These quantitative thresholds provide critical constraints for microphysical parameterizations, especially for high-altitude clouds where large supercooled droplets are frequently observed. Furthermore, SIP processes are governed by the dual regulation of temperature and hydrometeor concentrations. Temperature determines whether SIP can occur and which mechanism dominates; hydrometeor concentrations (drizzle, ice crystals, and precipitation particles) then modulate SIP intensity, exhibiting a pronounced positive correlation with the SIP ratio. In the lower temperature region, although HM is suppressed, DS and BR mechanisms can sustain certain SIP activity, maintaining relatively high ice concentrations.

https://doi.org/10.5194/egusphere-2026-4431
Preprint. Discussion started: 10 August 2026

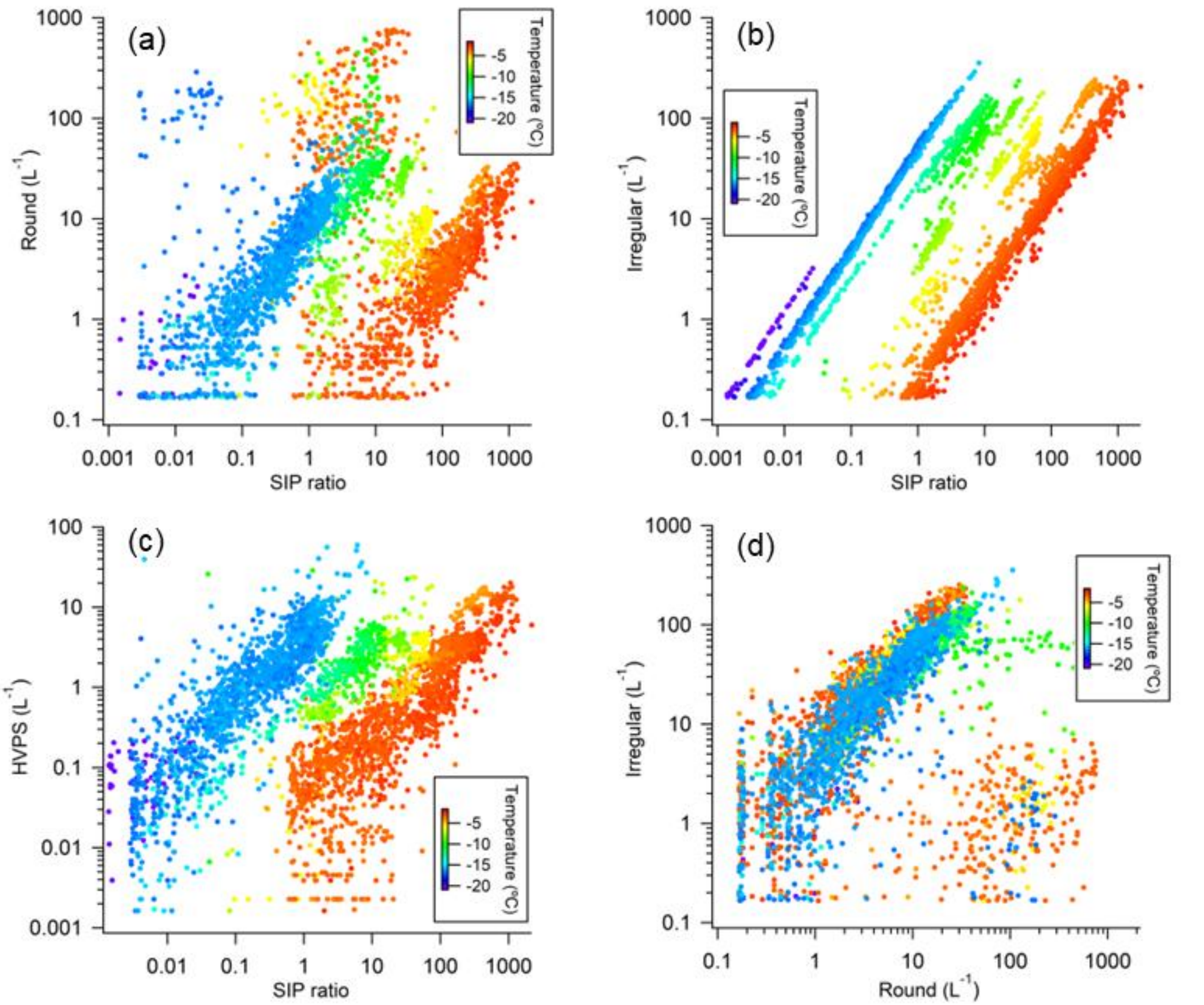

Figure 16: The number concentration of different particles as a function of SIP ratio (coloured with temperature): (a) SIP ratio vs drizzle, (b) SIP ratio vs irregular particle, (c) SIP ratio vs HVPS, (d) drizzle vs irregular particle.

4. Discussion

4.1 Comparison with other regions

Previous aircraft observations in China have mostly focused on the classic HM temperature window (−3℃ to −8℃) and tended to attribute high ice concentrations solely to the HM process (Yang et al., 2017; Zhao et al., 2023; Zhao and Lei, 2014). In recent years, Hou et al. (2023) and Long et al. (2025) suggested that in the embedded convective regions of

https://doi.org/10.5194/egusphere-2026-4431
Preprint. Discussion started: 10 August 2026

mixed-phase clouds, the BR process may coexist with the HM process, but their studies did not extend focus to temperatures outside the HM window. Wang et al. (2023) found that in mixed-phase clouds over eastern China, within the temperature range of −9°C to −15°C, the DS process could be the dominant source of secondary ice. Yang et al. (2014) reported the coexistence of multiple SIP mechanisms in nimbostratus over North China, suggesting that collisional breakup of dendritic crystals contributed to ice enhancement at −10°C to −15°C, while the HM and DS processes dominated between −3°C and −10°C. Recent studies have revealed the importance of DS and BR mechanisms outside the HM temperature range (Korolev et al., 2020, 2022; Huang et al., 2022). However, the reported ice multiplication factors are typically on the order of 10–100 (Sotiropoulou et al., 2020; Luke et al., 2021), which are substantially lower than the peak SIP ratio of 1000 observed over the TP. Moreover, previous studies have been largely limited to the identification of SIP phenomena and have not addressed the quantitative dependence of SIP intensity on temperature, hydrometeor concentrations and sizes.

Table 2 summarizes the SIP characteristics across different regions, illustrating that most studies are confined to or only slightly extend beyond the classic HM window. Therefore, the SIP observations over the TP in this study have three unique aspects. The effective temperature window for significant ice enhancement extended continuously from −3°C down to −16°C, which was considerably broader than the classic HM window and even wider than the recently reported extended range (−14°C in Du et al., 2024). Multiple SIP mechanisms (HM, DS, and BR) were identified within the same flight, and each SIP mechanism was supported by clear in-situ observational evidence. Moreover, the intensity of ice enhancement was relatively great, with the SIP ratio reaching up to 1000, indicating ice concentrations three orders of magnitude higher than the estimated INP concentrations. These distinctive features are likely attributable to three environmental factors specific to the TP. Firstly, the clean aerosol conditions minimize competition from primary nucleation, allowing SIP to dominate ice production. Secondly, strong convection maintains abundant supercooled liquid water, and the presence of large supercooled droplets and large dendritic snowflakes provides essential conditions for HM, DS, and BR. Thirdly, strong vertical updrafts can transport ice particles and large droplets from warmer levels to colder levels, extending the effective SIP temperature range through a seeder-feeder mechanism. The combination of these factors makes the TP a natural laboratory for studying efficient, broad-range SIP and provides important implications for improving cloud microphysical parameterizations over high-altitude regions.

Table 2. Comparison of SIP characteristics across different regions.

Region	Reported temperature and SIP mechanisms	Reported magnitude
TP convective cloud (this study, Zhao et al., 2023)	−3 to −8°C: signatures consistent with HM; DS and BR may coexist −8 to −16°C: DS, BR, and/or vertical transport	Maximum Nice is 205.4 L^{-1}; N_{ice}/N_{INP} up to 1000
Other region in China (Yang et al., 2014, 2017;	−3 to −8°C: HM-consistent signatures and possible BR	Different absolute concentrations and enhancement definitions; no

https://doi.org/10.5194/egusphere-2026-4431
Preprint. Discussion started: 10 August 2026

Hou et al., 2023; Wang et al., 2023; Long et al., 2025; Du et al., 2024)	−9 to −15°C: DS inferred in eastern China −10 to −15°C: possible BR of dendritic crystals	common ratio
Arctic mixed-phase clouds (Sotiropoulou et al., 2020; Luke et al., 2021)	−6.5 to −1.5°C: HM and BR required in case modelling Warmer than −10°C: drizzle-associated freezing fragmentation inferred from remote sensing	Model ice enhancement is 15−100; remote sensing ice multiplication up to 100 on average and rarely near 1000
UK weak convection (Crosier et al., 2011)	−5°C: signatures consistent with HM	More than 1 order above primary ice; no directly comparable N_{ice}/N_{INP} ratio
North American cloud systems (Lawson et al., 2017; Korolev et al., 2022)	−3 to −8°C: HM Below the HM range: several SIP mechanisms discussed Down to −27°C: SIP observed, but the specific mechanism was not be definitively identified	Source-specific absolute Nice and background enhancement; no comparable N_{ice}/N_{INP} ratio

4.2 Limitations and uncertainties

A fundamental limitation of this study is that the detailed mechanistic analysis of SIP, including the identification of specific mechanisms (HM, DS, BR), the derivation of droplet size thresholds for SIP initiation, and the examination of ice particle spectral evolution, is primarily based on a single well-observed flight case (06 July 2014). This case was selected because it exhibited the most comprehensive microphysical observations and the strongest SIP signatures, allowing for a robust process-level analysis. However, it is important to emphasize that the statistical dependences of the SIP ratio on temperature and hydrometeor concentrations, as presented in Section 3.3, are derived from all seven flights conducted during the TIPEX-III campaign (Figure S7), which consistently support the dual-regulation framework. Nonetheless, because the 06 July case represents a specific convective regime under clean aerosol conditions, the quantitative thresholds (e.g., 24 μm in the warm region and 200 μm in the cold region) and the relative contributions of individual SIP mechanisms may not be universally applicable to all cloud types or environmental conditions over the TP. Future campaigns with more extensive sampling across diverse convective regimes are needed to further validate and refine these findings.

Distinguishing the relative contributions of different SIP mechanisms from in-situ observations alone remains challenging, because the microphysical signatures of different mechanisms often overlap (Korolev and Leisner, 2020). While numerical modeling studies suggest that the dominant mechanism varies with temperature and cloud dynamics (Han et al., 2024;

https://doi.org/10.5194/egusphere-2026-4431
Preprint. Discussion started: 10 August 2026

Huang et al., 2022), direct observational attribution is inherently limited. Future work combining high-resolution models with coordinated aircraft measurements is needed to quantify the contribution of each mechanism.

A further source of uncertainty concerns the estimation of INP concentrations. The SIP ratio used in this study relies on the empirical parameterization of DeMott et al. (2010), which was developed from mid-latitude and oceanic data and may not fully represent the unique low-aerosol environment of the TP, especially at low temperatures. Given that the clean background aerosol concentrations over the TP are substantially lower than those used in the DeMott parameterization development, the estimated INP concentrations are likely overestimated, implying that the reported SIP ratios should be considered as conservative lower bounds of the actual ice enhancement. Despite these limitations, the observed ice enhancement and its environmental dependences are robust and provide useful constraints for improving microphysical parameterizations in high-altitude cloud models. These findings also highlight the urgent need for in situ INP measurements over the TP, particularly at temperatures below −10°C, to refine SIP efficiency assessments and to develop region-specific INP parameterizations.

5 Conclusions

In this study, the ice production in summer convective clouds over the TP was investigated based on aircraft observations from TIPEX-III. The main conclusions are as follows:

(1) A well-sampled convective clouds flight on 06 July 2014 exhibited strong ice enhancement signals. Ice concentrations in convective regions reached as high as 205.4 L^{-1}, exceeding estimated INP concentrations by 1–3 orders of magnitude. The effective temperature range for SIP extended to −16°C, substantially broader than the classical HM window (−3°C to −8°C). Within the HM temperature range, the SIP ratio peaked at 1000, indicating ice enhancement up to three orders of magnitude.

(2) Multiple SIP mechanisms may coexist and vary with temperature. In warmer convective regions (approximately −5°C), the HM process played the dominant role, accompanied by DS and BR. In colder regions (below −8°C), where HM became inefficient, the combined action of DS and BR sustained SIP, with strong updrafts potentially transporting ice particles and large droplets from warmer levels upward, further extending the effective SIP temperature window.

(3) Supercooled droplet size, rather than concentration alone, critically determined SIP initiation. Droplets larger than approximately 24 μm were sufficient to trigger SIP in the warm temperature range ($T > -8$°C), whereas the DS mechanism required droplets larger than approximately 200 μm to produce ice splinters upon freezing at colder temperatures ($T < -8$°C). Once the droplet size threshold is satisfied, higher droplet concentrations further enhance SIP intensity.

(4) Across seven flights, ice enhancement was governed by the dual regulation of temperature and hydrometeor concentrations. Temperature determined whether SIP occurred and which mechanism dominated, hydrometeor concentrations then modulated SIP intensity, exhibiting a pronounced positive correlation with the SIP ratio.

These findings provide new insights into the SIP processes in high-altitude convective clouds and have important implications for improving cloud microphysical parameterizations in weather and climate models. Compared with previous studies that attributed ice enhancement primarily to the HM process within the classic window (−3℃ and −8℃), our results demonstrate that the effective SIP temperature range over the TP extends to −16℃ through the coexistence of HM, DS, and BR mechanisms, with the SIP ratio reaching up to 1000, substantially higher than the enhancement factors in other regions. These advances highlight that the clean aerosol background over the TP fosters abundant supercooled droplets, which are critical for initiating and sustaining SIP. Future work should combine high-resolution numerical simulations to quantify their respective contributions and develop SIP parameterization schemes applicable to high altitude regions, providing scientific guidance for precise catalysis in weather modification operations over the TP.

Data availability

All in-situ aircraft data presented in this study are available from https://doi.org/10.17632/xwtrzt7mvy.1 (Long, 2026).

Author contributions

YY, DL, YZ and DT designed the research. DL and MY prepared and provided measurement datasets. The paper was written by YY with guidance from DL, YZ, DT, and JD. All the authors read and improved the manuscript.

Competing interests

At least one of the (co-)authors is a member of the editorial board of Atmospheric Chemistry and Physics.

Acknowledgements

The authors gratefully acknowledge to Beijing Weather Modification Center for their outstanding cooperation during in situ data collection during the Third Tibetan Plateau Atmospheric Scientific Experiment (TIPEX-III).

Financial support

This research has been supported by Science & Technology Fundamental Resources Investigation Program (Grant No. 2025FY101502), the National Natural Science Foundation of China (Grant No. 4257050694) and the China Meteorological Administration Innovation and Development Program (Grant No. CXFZ2025J038).

https://doi.org/10.5194/egusphere-2026-4431
Preprint. Discussion started: 10 August 2026

References

Bailey, M. P. and Hallett, J.: A Comprehensive Habit Diagram for Atmospheric Ice Crystals: Confirmation from the Laboratory, AIRS II, and Other Field Studies, J. Atmos. Sci., 66, 2888–2899, https://doi.org/10.1175/2009JAS2883.1, 2009.

Bony, S., Stevens, B., Frierson, D. M. W., Jakob, C., Kageyama, M., Pincus, R., Shepherd, T. G., Sherwood, S. C., Siebesma, A. P., Sobel, A. H., Watanabe, M., and Webb, M. J.: Clouds, circulation and climate sensitivity, Nature Geosci, 8, 261–268, https://doi.org/10.1038/ngeo2398, 2015.

Cantrell, W. and Heymsfield, A.: Production of ice in tropospheric clouds: A review, Bull. Amer. Meteor. Soc., 86, 795–807, https://doi.org/10.1175/BAMS-86-6-795, 2005.

Chang, Y., Guo, X., Tang, J., and Lu, G.: Aircraft measurement campaign on summer cloud microphysical properties over the Tibetan Plateau, Sci. Rep., 9, 4912, https://doi.org/10.1038/s41598-019-41514-5, 2019.

Crawford, I., Bower, K. N., Choularton, T. W., Dearden, C., Crosier, J., Westbrook, C., Capes, G., Coe, H., Connolly, P. J., Dorsey, J. R., Gallagher, M. W., Williams, P., Trembath, J., Cui, Z., and Blyth, A.: Ice formation and development in aged, wintertime cumulus over the UK: observations and modelling, Atmos. Chem. Phys., 12, 4963–4985, https://doi.org/10.5194/acp-12-4963-2012, 2012.

Crosier, J., Bower, K. N., Choularton, T. W., Westbrook, C. D., Connolly, P. J., Cui, Z. Q., Crawford, I. P., Capes, G. L., Coe, H., Dorsey, J. R., Williams, P. I., Illingworth, A. J., Gallagher, M. W., and Blyth, A. M.: Observations of ice multiplication in a weakly convective cell embedded in supercooled mid-level stratus, Atmos. Chem. Phys., 11, 257–273, https://doi.org/10.5194/acp-11-257-2011, 2011.

DeMott, P. J., Prenni, A. J., Liu, X., Kreidenweis, S. M., Petters, M. D., Twohy, C. H., Richardson, M. S., Eidhammer, T., and Rogers, D. C.: Predicting global atmospheric ice nuclei distributions and their impacts on climate, Proc. Natl. Acad. Sci., 107, 11217–11222, https://doi.org/10.1073/pnas.0910818107, 2010.

Du, Y., Liu, D., Zhao, D., Huang, M., Tian, P., Wen, D., Xiao, W., Zhou, W., He, H., Pan, B., Zuo, D., Liu, X., Jing, Y., Zhang, R., Sheng, J., Wang, F., Huang, Y., Chen, Y., and Ding, D.: Microphysical view of the development and ice production of mid-latitude stratiform clouds with embedded convection during an extratropical cyclone, Atmos. Chem. Phys., 24, 13429–13444, https://doi.org/10.5194/acp-24-13429-2024, 2024.

Field, P. R., Lawson, R. P., Brown, P. R. A., Lloyd, G., Westbrook, C., Moisseev, D., Miltenberger, A., Nenes, A., Blyth, A., Choularton, T., Connolly, P., Buehl, J., Crosier, J., Cui, Z., Dearden, C., DeMott, P., Flossmann, A., Heymsfield, A., Huang, Y., Kalesse, H., Kanji, Z. A., Korolev, A., Kirchgaessner, A., Lasher-Trapp, S., Leisner, T., McFarquhar, G., Phillips, V., Stith, J., and Sullivan, S.: Secondary Ice Production: Current State of the Science and Recommendations for the Future, Meteor. Monogr., 58, 7.1-7.20, https://doi.org/10.1175/AMSMONOGRAPHS-D-16-0014.1, 2017.

Glienke, S. and Mei, F.: Cloud Particle Imager (CPI) and 3-View Cloud Particle Imager (3V-CPI) Instrument Handbook, DOE/SC-ARM-TR-240, 13 pp., U.S. Department of Energy Office of Scientific and Technical Information, https://doi.org/10.2172/1597645, 2020.

Griggs, D. J. and Choularton, T. W.: Freezing modes of riming droplets with application to ice splinter production, Q. J. Roy. Meteorol. Soc., 109, 243–253, https://doi.org/10.1002/qj.49710945912, 1983.

https://doi.org/10.5194/egusphere-2026-4431
Preprint. Discussion started: 10 August 2026

Grosvenor, D. P., Choularton, T. W., Lachlan-Cope, T., Gallagher, M. W., Crosier, J., Bower, K. N., Ladkin, R. S., and Dorsey, J. R.: In-situ aircraft observations of ice concentrations within clouds over the Antarctic Peninsula and Larsen Ice Shelf, Atmos. Chem. Phys., 12, 11275–11294, https://doi.org/10.5194/acp-12-11275-2012, 2012.

Guo, X., Fu, D., Li, X., Hu, Z., Lei, H., Xiao, H., and Hong, Y.: Advances in cloud physics and weather modification in China, Adv. Atmos. Sci., 32, 230–249, https://doi.org/10.1007/s00376-014-0006-9, 2015.

Hallett, J. and Mossop, S. C.: Production of secondary ice particles during the riming process, Nature, 249, 26–28, https://doi.org/10.1038/249026a0, 1974.

Han, C., Hoose, C., and Dürlich, V.: Secondary Ice Production in Simulated Deep Convective Clouds: A Sensitivity Study, J. Atmos. Sci., 81, 903–921, https://doi.org/10.1175/JAS-D-23-0156.1, 2024.

Hou, T., Chen, B., Zhou, X., Zhao, C., Feng, Q., Yan, F., Zhou, W., Cui, Y., Du, Y., Li, Z., Zhao, D., and Ma, X.: Aircraft-based observations of ice concentrations in a midlatitude mixed-phase stratiform cloud system with embedded convection, Atmos. Res., 281, 106471, https://doi.org/10.1016/j.atmosres.2022.106471, 2023.

Hou, T., Lei, H., He, Y., Yang, J., Zhao, Z., and Hu, Z.: Aircraft Measurements of the Microphysical Properties of Stratiform Clouds with Embedded Convection, Adv. Atmos. Sci., 38, 966–982, https://doi.org/10.1007/s00376-021-0287-8, 2021.

Huang, Y., Blyth, A. M., Brown, P. R. A., Choularton, T. W., Connolly, P., Gadian, A. M., Jones, H., Latham, J., Cui, Z., and Carslaw, K.: The development of ice in a cumulus cloud over southwest England, New J. Phys., 10, 105021, https://doi.org/10.1088/1367-2630/10/10/105021, 2008.

Huang, Y., Blyth, A. M., Brown, P. R. A., Cotton, R., Crosier, J., Bower, K. N., Gallagher, M. W., Jones, H., Gadian, A. M., Choularton, T. W., Cardwell, J., Coe, H., Mobbs, S. D., and Hagen, M.: Development of ice particles in convective clouds observed over the Black Forest mountains during COPS, Q. J. Roy. Meteorol. Soc., 137, 275–286, https://doi.org/10.1002/qj.749, 2011.

Huang, Y., Wu, W., McFarquhar, G. M., Xue, M., Morrison, H., Milbrandt, J., Korolev, A. V., Hu, Y., Qu, Z., Wolde, M., Nguyen, C., Schwarzenboeck, A., and Heckman, I.: Microphysical processes producing high ice water contents (HIWCs) in tropical convective clouds during the HAIC-HIWC field campaign: dominant role of secondary ice production, Atmos. Chem. Phys., 22, 2365–2384, https://doi.org/10.5194/acp-22-2365-2022, 2022.

Kang, S., Xu, Y., You, Q., Flügel, W.-A., Pepin, N., and Yao, T.: Review of climate and cryospheric change in the Tibetan Plateau, Environ. Res. Lett., 5, 015101, https://doi.org/10.1088/1748-9326/5/1/015101, 2010.

Knight, C. A.: Ice Growth from the Vapor at −5°C, J. Atmos. Sci., 69, 2031–2040, https://doi.org/10.1175/JAS-D-11-0287.1, 2012.

Korolev, A. and Isaac, G. A.: Shattering during Sampling by OAPs and HVPS. Part I: Snow Particles, J. Atmos. Ocean. Tech., 22, 528–542, https://doi.org/10.1175/JTECH1720.1, 2005.

Korolev, A. and Leisner, T.: Review of experimental studies of secondary ice production, Atmos. Chem. Phys., 20, 11767–11797, https://doi.org/10.5194/acp-20-11767-2020, 2020.

Korolev, A. V., Strapp, J. W., Isaac, G. A., and Nevzorov, A. N.: The Nevzorov airborne hot-wire LWC–TWC probe: Principle of operation and performance characteristics, J. Atmos. Oceanic Technol., 15, 1495–1510, https://doi.org/10.1175/1520-0426(1998)015<<1495:TNAHWL>2.0.CO;2, 1998.

Korolev, A., DeMott, P. J., Heckman, I., Wolde, M., Williams, E., Smalley, D. J., and Donovan, M. F.: Observation of secondary ice production in clouds at low temperatures, Atmos. Chem. Phys., 22, 13103–13113, https://doi.org/10.5194/acp-22-13103-2022, 2022.

Korolev, A., Heckman, I., Wolde, M., Ackerman, A. S., Fridlind, A. M., Ladino, L. A., Lawson, R. P., Milbrandt, J., and Williams, E.: A new look at the environmental conditions favorable to secondary ice production, Atmos. Chem. Phys., 20, 1391–1429, https://doi.org/10.5194/acp-20-1391-2020, 2020.

Korolev, A., McFarquhar, G., Field, P. R., Franklin, C., Lawson, P., Wang, Z., Williams, E., Abel, S. J., Axisa, D., Borrmann, S., Crosier, J., Fugal, J., Krämer, M., Lohmann, U., Schlenczek, O., Schnaiter, M., and Wendisch, M.: Mixed-Phase Clouds: Progress and Challenges, Meteor. Monogr., 58, 5.1-5.50, https://doi.org/10.1175/AMSMONOGRAPHS-D-17-0001.1, 2017.

Lance, S., Brock, C. A., Rogers, D., and Gordon, J. A.: Water droplet calibration of the Cloud Droplet Probe (CDP) and in-flight performance in liquid, ice and mixed-phase clouds during ARCPAC, Atmospheric Meas. Tech., 3, 1683–1706, https://doi.org/10.5194/amt-3-1683-2010, 2010.

Lauber, A., Kiselev, A., Pander, T., Handmann, P., and Leisner, T.: Secondary Ice Formation during Freezing of Levitated Droplets, J. Atmos. Sci., 75, 2815–2826, https://doi.org/10.1175/JAS-D-18-0052.1, 2018.

Lawson, P., Gurganus, C., Woods, S., and Bruintjes, R.: Aircraft Observations of Cumulus Microphysics Ranging from the Tropics to Midlatitudes: Implications for a “New” Secondary Ice Process, J. Atmos. Sci., 74, 2899–2920, https://doi.org/10.1175/JAS-D-17-0033.1, 2017.

Lawson, R. P., O’Connor, D., Zmarzly, P., Weaver, K., Baker, B., Mo, Q., and Jonsson, H.: The 2D-S (Stereo) probe: Design and preliminary tests of a new airborne, high-speed, high-resolution particle imaging probe, J. Atmos. Ocean. Technol., 23, 1462–1477, https://doi.org/10.1175/JTECH1927.1, 2006.

Leisner, T.: Secondary ice processes upon heterogeneous freezing of cloud droplets, 14th Conf. on Cloud Physics and 14th Conf. on Atmospheric Radiation (Joint with the 2nd Anthony J. Slingo Symposium), Boston, MA, Amer. Meteor. Soc., 7.3, https://ams.confex.com/ams/14CLOUD14ATRAD/webprogram/Paper252981.html, 2014.

Liu, X. and Chen, B.: Climatic warming in the Tibetan Plateau during recent decades, Int. J. Climatol., 20, 1729–1742, https://doi.org/10.1002/1097-0088(20001130)20:14%3C1729::AID-JOC556%3E3.0.CO;2-Y, 2000.

Long, Y., Hou, T., Chen, B., Xi, L., Hua, S., Chang, Y., Zhang, B., and Zhao, D.: Ice Particle Size Distributions and Secondary Ice Production in Stratiform Clouds Over the Qilian Mountains in Northwestern China, J. Geophys. Res.-Atmos., 130, e2025JD043608, https://doi.org/10.1029/2025JD043608, 2025.

Long, Y.: Aircraft data over the Tibetan Plateau, Mendeley Data [Dataset], https://doi.org/10.17632/xwtrzt7mvy.1, 2026.

Luke, E. P., Yang, F., Kollias, P., Vogelmann, A. M., and Maahn, M.: New insights into ice multiplication using remote-sensing observations of slightly supercooled mixed-phase clouds in the Arctic, Proc. Natl. Acad. Sci. U.S.A., 118, e2021387118, https://doi.org/10.1073/pnas.2021387118, 2021.

Mossop, S. C.: Microphysical properties of supercooled cumulus clouds in which an ice particle multiplication process operated, Quart J Royal Meteoro Soc, 111, 183–198, https://doi.org/10.1002/qj.49711146708, 1985.

https://doi.org/10.5194/egusphere-2026-4431
Preprint. Discussion started: 10 August 2026

Qiu, Y., Lu, C., and Luo, S.: Tibetan Plateau Cloud Structure and Cloud Water Content Derived from Millimeter Cloud Radar Observations in Summer, Pure Appl. Geophys., 176, 1785–1796, https://doi.org/10.1007/s00024-018-2034-3, 2019.

Rangno, A. L. and Hobbs, P. V.: Ice particles in stratiform clouds in the Arctic and possible mechanisms for the production of high ice concentrations, J. Geophys. Res.-Atmos., 106, 15065–15075, https://doi.org/10.1029/2000JD900286, 2001.

Sotiropoulou, G., Sullivan, S., Savre, J., Lloyd, G., Lachlan-Cope, T., Ekman, A. M. L., and Nenes, A.: The impact of secondary ice production on Arctic stratocumulus, Atmos. Chem. Phys., 20, 1301–1316, https://doi.org/10.5194/acp-20-1301-2020, 2020.

Suo, X., Yu, Z., and Cao, S.: Utilizing water resources from the Tibetan Plateau: Benefits, risks, and future research requirements, Catena, 230, 107256, https://doi.org/10.1016/j.catena.2023.107256, 2023.

Takahashi, T., Nagao, Y., and Kushiyama, Y.: Possible high ice particle production during graupel–graupel collisions, J. Atmos. Sci., 52, 4523–4527, https://doi.org/10.1175/1520-0469(1995)052<4523:PHIPPD>2.0.CO;2, 1995.

Vardiman, L.: The Generation of Secondary Ice Particles in Clouds by Crystal–Crystal Collision, J. Atmos. Sci., 35, 2168–2180, https://doi.org/10.1175/1520-0469(1978)035%3C2168:TGOSIP%3E2.0.CO;2, 1978.

Waman, D., Patade, S., Jadav, A., Deshmukh, A., Gupta, A. K., Phillips, V. T. J., Bansemer, A., and DeMott, P. J.: Dependencies of Four Mechanisms of Secondary Ice Production on Cloud-Top Temperature in a Continental Convective Storm, J. Atmos. Sci., 79, 3375–3404, https://doi.org/10.1175/JAS-D-21-0278.1, 2022.

Wang, Y., Kong, R., Cai, M., Zhou, Y., Song, C., Liu, S., Li, Q., Chen, H., and Zhao, C.: High small ice concentration in stratiform clouds over Eastern China based on aircraft observations: Habit properties and potential roles of secondary ice production, Atmospheric Research, 281, 106495, https://doi.org/10.1016/j.atmosres.2022.106495, 2023.

Wieder, J., Ihn, N., Mignani, C., Haarig, M., Bühl, J., Seifert, P., Engelmann, R., Ramelli, F., Kanji, Z. A., Lohmann, U., and Henneberger, J.: Retrieving ice-nucleating particle concentration and ice multiplication factors using active remote sensing validated by in situ observations, Atmos. Chem. Phys., 22, 9767–9797, https://doi.org/10.5194/acp-22-9767-2022, 2022.

Wildeman, S.: Fast Dynamics of Water Droplets Freezing from the Outside In, Phys. Rev. Lett., 118, https://doi.org/10.1103/PhysRevLett.118.084101, 2017.

Yang, J., Lei, H., and Hou, T.: Observational evidence of high ice concentration in a shallow convective cloud embedded in stratiform cloud over North China, Adv. Atmos. Sci., 34, 509–520, https://doi.org/10.1007/s00376-016-6079-x, 2017.

Yang, J., Lei, H., Hu, Z., and Hou, T.: Particle size spectra and possible mechanisms of high ice concentration in nimbostratus over Hebei Province, China, Atmos. Res., 142, 79–90, https://doi.org/10.1016/j.atmosres.2013.12.018, 2014.

Zhao, C., Liu, L., Wang, Q., Qiu, Y., Wang, W., Wang, Y., and Fan, T.: Toward Understanding the Properties of High Ice Clouds at the Naqu Site on the Tibetan Plateau Using Ground-Based Active Remote Sensing Measurements Obtained during a Short Period in July 2014, J. Appl. Meteorol. Climatol., **56**, 551–566, https://doi.org/10.1175/JAMC-D-16-0038.1, 2016.

Zhao, C., Liu, L., Wang, Q., Qiu, Y., Wang, Y., and Wu, X.: MMCR-based characteristic properties of non-precipitating cloud liquid droplets at Naqu site over Tibetan Plateau in July 2014, Atmos. Res., 190, 68–76, https://doi.org/10.1016/j.atmosres.2017.02.002, 2017.

Zhao, D., Wang, M., Rosenfeld, D., Chen, B., Liu, D., Wu, X., Hu, K., Ding, S., Zhu, Y., Zeng, Y., Qu, Y., Gao, Y., Bi, K., Du, Y., Huang, M., He, H., and Ding, D.: Aircraft observation of fast initiation of mixed phase precipitation in convective cloud over the Tibetan Plateau, Atmos. Res., 285, 106627, https://doi.org/10.1016/j.atmosres.2023.106627, 2023.

Zhao, P., Xu, X., Chen, F., Guo, X., Zheng, X., Liu, L., Hong, Y., Li, Y., La, Z., Peng, H., Zhong, L., Ma, Y., Tang, S., Liu, Y., Liu, H., Li, Y., Zhang, Q., Hu, Z., Sun, J., Zhang, S., Dong, L., Zhang, H., Zhao, Y., Yan, X., Xiao, A., Wan, W., Liu, Y., Chen, J., Liu, G., Zhaxi, Y., and Zhou, X.: The Third Atmospheric Scientific Experiment for Understanding the Earth–Atmosphere Coupled System over the Tibetan Plateau and Its Effects, Bull. Amer. Meteor. Soc., 99, 2493–2515, https://doi.org/10.1175/BAMS-D-16-0050.1, 2018.

Zhao, X. and Liu, X.: Global Importance of Secondary Ice Production, Geophys. Res. Lett., 48, e2021GL092581, https://doi.org/10.1029/2021GL092581, 2021.

Zhao, Z. and Lei, H.: Observed microphysical structure of nimbostratus in northeast cold vortex over China, Atmos. Res., 142, 91–99, https://doi.org/10.1016/j.atmosres.2013.09.008, 2014.